HIGH TEMPORAL RESOLUTION RADAR OBSERVATIONS OF VARIOUS SCATTERERS IN THE ATMOSPHERE AT 10 GHZ: EXPERIENCES IN MEDITERRANEAN SEMI-ARID REGIONS AND IN THE WESTERN ALPS

M. Gabella[1], E. Morin[2], A. Leuenberger[1], R. Notarpietro[3,4], M. Branca[4], J. Figueras[1], M. Schneebeli[1], U. Germann[1]

[1]Radar Satellite and Nowcasting, MeteoSwiss, via ai Monti 146, CH-6605 Locarno Monti, Switzerland.
[2]Department of Geography, The Hebrew University of Jerusalem, Jerusalem, Israel.
[3]Electronics Department, Politecnico di Torino, Torino, Italy.
Corresponding author: Marco Gabella, Phone +41-91-7562319, marco.gabella@meteoswiss.ch

Session: Developments in observing technologies.

Abstract

Radar is a unique tool to get real time overview on the current weather situation; however, high spatial resolution observations can only be achieved at short ranges, the angular resolution being an important limiting factor. How to tackle the emerging needs for high spatio-temporal resolution? Short-range, fast-scanning, X-band, mini radars can be a solution, especially for monitoring in details small basins prone to flash flood, towns and valleys. Cost, radiation and installation issues motivate the use of small antennas that can easily be installed on existing infrastructures or even on a truck.

The paper presents lessons gained in various climates and with different X-band systems: low-cost, portable, single elevation, 10 kW systems delivering one precipitation map per minute as well as a sophisticated, fast 3D scanning, 75 kW Doppler, polarimetric radar on wheel aiming at the detection of both distributed (precipitation particles) and isolated scatterers (airplanes). The areas under surveillance include complex orography regions in the “wet” Western Alps and in the Be'er Sheva semi-arid region (Israel).

Preliminary results shows the advantages of sampling precipitation fields once per minute with high spatial resolution, hence obtaining detailed real-time observations; additional Doppler and polarimetric information are highly beneficial (but system costs are one order of magnitude larger). Main challenges and open points are related to attenuation along the path and/or wet-radome attenuation.

1 Introduction

Meteorological radar is a unique tool to get real time overview on the current precipitation fields: it clearly shows where and when something is happening; however, to precisely describe what is happening is far more difficult. This is not because we miss careful investigations, but simply, because radar can only see the hydrometeors aloft, while we would need to know what is arriving at ground level. Obstacles as well as earth curvature lead to a limited horizon, allowing us to see precipitation at variable height, often too far from the ground. The situation becomes obviously much more difficult in mountainous terrain, where weather echoes can only be detected at high altitudes because of beam shielding by relieves: there, terrain blockage combined with the shallow depth of precipitation during cold seasons and low melting levels causes inadequate radar coverage for quantitative precipitation estimation (QPE), especially in narrow valleys.

All these difficulties increase rapidly with distance from the radar location: high spatial resolution observations can only be achieved at short ranges, the angular resolution (i.e., the antenna size) being one of the main limiting factors. The monostatic radar backscattering sampling volume increases, in fact, with the square of the range. Perhaps, accurate QPE can only be achieved at short ranges from the radar: at short ranges, we may even get good quantitative data. But at longer ranges it may be impossible to obtain the desired precision, e.g. the precision needed to alert people living in small catchments in complex orography regions. Indeed, the precipitation field is too variable for the “coarse” resolution of long-range radars. The variability of natural precipitation is so large that the radar beam is often not able to resolve it. As a result we find aloft different types of particles and non-homogeneous reflectivity in the pulse volume, to be compared with rain rate at the ground level. The under-sampling problem becomes increasingly severe with increasing ranges; therefore, at longer ranges, small but intense features of the precipitation system are blurred (non-

homogeneous beam filling). Furthermore, it is more likely to include different types of hydrometeors (e.g., snow, ice, and rain drops), especially in the vertical dimension.
In mountainous terrain, precipitation is even more variable both in space and time because of orographic effects and interactions of mountains with wind fields. This variability within the scattering volume is in contradiction with the homogeneously filled pulse volume assumption usually made when considering the meteorological radar equation. Fulfilling the assumption of homogeneous beam filling, however, is a prerequisite for a precise estimate of reflectivity, attenuation and phase shift along the beam.
Long-range radar networks remain an essential part of the weather forecasting and warning infrastructures used by many countries worldwide. Despite significant capability and continuous improvement, a limitation of current weather radar networks is the inability to observe the lower part of the atmosphere and detect fine-scale weather features. Designed for long-range coverage through precipitation, these radars must operate at radar wavelengths that are not affected by attenuation. This implies the use of large antennas and high-power transmitters (to meet sensitivity requirements at long ranges); up to now, such large antennas are mechanically scanned, hence requiring dedicated land, towers and other support infrastructures.
How to tackle the emerging need for improved low-altitude coverage and high temporal-resolution weather radars? Low-cost, fast-scanning, short-range X-band radars for precipitation monitoring can be a valid solution for complementing long-range radars, especially in the following environments:

- heavily populated areas (e.g. Torino town and outskirts, Italy, see Sec. 3.3);
- specific dry and semi-arid regions prone to flash flood, where it is crucial to improve observation of low-level meteorological phenomena (e.g. Be'er Sheva region, Israel, see Sec 3.4);
- deep valleys surrounded by mountains (e.g. Locarno and Meiringen, Switzerland, see Sec. 5).

This study is organized in several sections: Section 2 introduces the scores used to assess the agreement between remotely sensed (radar) estimates and in situ (rain gauges) observations. Section 3 presents QPE performances obtained with low-cost, short-range, X-band radars. Section 4 show QPE results obtained with a conventional, C-band radar network; it is a useful benchmark to set the results of Sec. 3 in context. Sec. 5 presents results obtained with an innovative sensor: a polarimetric, Doppler, mobile, X-band radar. Section 6 summarizes the lesson gained and presents conclusions.

2 Quantitative Precipitation Estimation (QPE) assessment

In the following Sections 3 and 4, we will present daily radar-derived precipitation amounts as obtained from weather echoes aloft (using various volume sizes) to be compared with point measurements acquired at the ground by rain gauges.

The assessment is based by looking at the average value and the dispersion of the errors (we call error the disagreement between radar and gauge amounts). For such characterization, we define the two following parameters:

1. **Bias** (in **dB**). The bias in dB is defined as the ratio between radar and gauge total precipitation amounts on a logarithmic (decibel) scale. It describes the overall agreement between radar estimates and ground point measurements. It is averaged over the whole space–time window of the sample. A positive (negative) bias in dB denotes an overall radar overestimation (underestimation).
2. **Scatter** (in **dB**). The definition of scatter is strictly connected to the selected error distribution from a hydrological (end-user) and radar-meteorological (remotely sensed samples of the spatio-temporal variability of the precipitation field) perspective. The error distribution is expressed as the cumulative contribution to total rainfall (hydrologist point of view, y axis) as a function of the radar–gauge ratio (radar-meteorologist point of view, x axis). An example of the error distribution is shown in Fig. 2 and 3 of *Germann et al.* [2004]. The scatter is defined as half the distance between the 16% and 84% percentiles of the “weighted” error-distribution.

From our radar-meteorological point of view the multiplicative nature of the error prevails with respect to the additive one. For example, water on the radome, a wrong calibration radar constant, a bad estimate of the vertical profile …, all result in a multiplicative error (i.e. a factor) rather than an additive error (i.e. a difference). This is why bias, error distribution and scatter are expressed as ratios in dB. The scatter as defined above is a robust measure of the spread. It is insensitive to outliers in two ways. First, each radar–gauge pair is weighted by its contribution to total rainfall (y axis of the cumulative error distribution). An ill-

defined large ratio that results from two small values, e.g. 0.4 mm/2 mm ~ −7 dB, describes an irrelevant event from a hydrological point of view, and only gets little weight. Second, by taking the distance between the 16% and the 84% percentiles, the tails of the error distribution are not overrated. Another important advantage of the spread measure is that it is unaffected by the bias error, hence providing a complementary view of the error in the estimates.
Furthermore, as an additional simple and effective measurement of agreement, we will provide the percentage of the explained variance, which is the square of the radar-gauge pairs correlation coefficient multiplied by a hundred.

3 QPE using single-elevation, short-range, low-cost, X-band radars

Cost, radiation safety issues and aesthetic issues motivate the use of small antennas and low-power transmitters that could be installed on either low-cost towers or existing infrastructures such as rooftops of existing buildings or telecommunication poles. This requires that the radars are physically small and that the radiated power levels are low enough such that no actual or perceived radiation safety hazard is imposed. We have opted for a quite small parabolic antenna (D~0.6 m) which corresponds to a 3 dB cross-range spatial resolution of 1 km at 20 km range (two third of the used range, which is 30 km). The antenna is protected by a ~1 m diameter radome and rotates at ~132° per second (using a single elevation). The low-cost mini-radar has important limitation compared to more expensive and high-performance system: it is non-Doppler, single elevation and single-polarization. Nevertheless, an important advantage of such system is certainly its high temporal resolution.

3.1 High temporal resolution

As stated, a clear advantage of the low-cost X-band radar is its high temporal resolution: currently it delivers a polar image of precipitation every minute by averaging 9 consecutive rays and then 16 rotations (out of the 22 available), hence resulting in a total of 144 samples. However, the temporal resolution could be reduced to 30 s (or even 15 s), if one could cope with 72 (36) samples.
In all field campaign here presented, the mini-radar has been run with the configuration listed in Table 1.

Frequency	X-Band (9.4 GHz)
Range	up to 30 km
Power	10 kW
Pulse duration	400 ns
Pulse Repetition Frequency	800 Hz
Scan program	Single elevation, 3.6° half power beam width, horizontal pol.
Antenna	0.6 m diameter parabolic reflector

Table 1. Main characteristics of the low-cost weather radar.

For each radar bin (400 ns pulse width; 3.6° Half Power Beam Width), how is a “polar” (i.e. range-azimuth), “1-minute-sampled”, radar reflectivity value obtained? Within each azimuthal 3.6° HPBW, there are slightly more than 21 pulses, which are separated by the 1.25 ms pulse repetition interval; among them, only 9 (“most-central”) consecutive shots are selected and averaged at every antenna revolution (2.727 s). Every minute, in fact, the antenna performs 22 revolutions; however only data from the first 16 revolutions are averaged on a linear power scale (algebraic average: dBm values are antilog transformed, then averaged, then again transformed on a decibel logarithmic scale). This means a total of 144 (9 times 16) samples, of which 32 are independent, if we assume a decorrelation time of ~10 ms (Fig. 1.14, *Sauvageot* [1992]): the first and last sample, of the 9 consecutive rays are in fact separated by 9×1.25 = 11.25 ms.
It is well known that the backscattered power caused by raindrops is, unfortunately, only indirectly linked to the rain rate, R, where [R] = mm/h. The backscattered power caused by the hydrometeors and detected by the radar is, in fact, directly proportional to the radar reflectivity factor, Z, where [Z] = mm^6/m^3. Here we have used a single Z-R relationship to derive the variable of interest, R, from the geophysical observable, Z, which is detected by the meteorological radar. More details regarding this simplifying assumption can be found in Section 4 of *Gabella et al.* [2011]. For each radar bin, a maximum of 1440 clutter-free radar reflectivity values

per day are then transformed into “instantaneous” rain rate, R, and then added to derive the corresponding daily-accumulated value presented in this study.

3.2 Selected Area-Time Integral: daily accumulation and various areal sizes

The structure of precipitation fields has long been studied and their large variability in time and space recognized. In fact, rainfall rate at the ground can easily vary by a factor of 10 within a 10 min period or within 2 km distance. The small-scale variability of precipitation is clearly shown by radar rainfall measurements. Such variability and the large differences in sampling modes are relevant when comparing measurements from radar and rain gauges: the radar sampling once every few minutes a volume high up in the sky (a volume that increases in size with the square of the range), and the rain gauge recording continuously at a single point on the ground; the interested reader can find an extensive and detailed study regarding the radar-gauge comparison in *Zawadzki* [1975].
Assuming an average fall velocity of rain of 5 m/s and an area of the gauge of 200 cm^2, the gauge samples in ten minutes a volume as small as 60 m^3; on the contrary, at the average radar-gauges distance listed in Section 3 (~19.5 km), both the Torino and Gilat X-band radars sample an instantaneous volume of the order of 7×10^7! m^3. At the average radar-gauges distance listed in Section 4.1.1 (16 km range, on average), the C-band Lema radar samples a volume of the order of 0.6×10^7 m^3; for Dole (Section 4.1.2) and Albis C-band radars the averaged sample volume is of the order of 1.6×10^7 m^3. Even from this simple and basic considerations, it is evident that the radar-gauge comparison is problematic, as shown in many papers. As an example, we here report two sentences from the “Summary and conclusions” section in the famous paper by *Pauline Austin* [1987]:

- “Very often large and apparently random discrepancies between radar-indicated rainfall and amounts collected by a single rain gauge and they are attributed to differences in sampling modes”.
- “… the spatial variability of rainfall is so pronounced that a single gauge often does not sample representatively over an area, even one as small as 4 km^2.”

On the one hand, it would be advisable not to downgrade the spatial resolution obtainable by the radar. On the other hand, it is not possible to precisely identify the radar pixel to be put in relation with a given gauge, mainly because of wind effects (variable intensity and direction!): large drops have larger terminal fall velocities than smaller one; hence, they reach the ground closer to the Nadir of the precipitating cloud, where they had been remotely sensed by the radar wave.
This is the reason why in the present study the radar daily amounts have been derived by averaging linear radar reflectivity values over different spatial domains: 0.1 km^2, 0.25 km^2, 1 km^2 and 25 km^2.

3.3 QPE performances for the Torino radar (Italy): April-May 2013

The Torino radar is located on the roof of the Politecnico di Torino (Electronics and Telecommunications Department): its latitude is 45°.063; the longitude is 7°.660; the altitude is 275 m above Mean Sea Level (MSL). For the quantitative evaluation of the radar estimates we have been using **six** rain gauges of the Weather Underground network: five of them have distances from the radar between 19 and 23 km; the last one is at 12 km range; their average (±standard deviation) distance from the radar site is 19.5±4.1 km. April and May 2013 have been particularly rainy (not surprisingly, climatologically these are the two months with more rain), so that we could analyze **28** rainy days; during such days, the average daily precipitation is 15.0 (12.9) mm according to gauges (0.1 km^2 radar estimates aloft), which corresponds to an “overall Bias” of -0.67 dB (radar underestimation, see also Table 3.3.2a). The corresponding Coefficient of Variation (relative dispersion) is 0.99 (0.89) mm according to gauges (radar). Out of the available **168** daily amounts, 151 were classified as wet according to gauges (G>0.5 mm/day), while 149 were classified as wet (R>0.2 mm/day) according to the radar (see also Table 2). In 145 cases out of 168, both the radar estimate and corresponding gauge measurement at the ground agree in classifying the day as “wet”: this indicate a relatively homogenous wet situation at the selected daily integration period.

3.3.1 Radar-based wet vs dry discrimination (in rainy days) using the gauge as reference

The history of applying contingency tables (also called error matrices in the remote sensing field) for the verification of one set of observations against a reference set is a quite long one. The history of categorical

statistics based on such tables is rather fascinating and an interesting account is given by Murphy (1996). Most of the scores were first derived nearly a century ago and have been rediscovered several times (with different names in different branches of science, see for instance the bullet list below).
The dimension of the contingency tables can be as small as 2 by 2 (tetrachoric) or larger (polychoric) depending on the number of thresholds used in the classification scheme. Obviously, in our wet-versus-dry hourly values discrimination, we are dealing with tetrachoric tables, since just one discrete value (namely 0.4 mm/h) is used to divide the two categories. On the one hand, the properties of a set of observations can be condensed and clearly displayed through such tables; on the other hand, to satisfy needs of specific users, even for a simple tetrachoric table, several different scores have been introduced.
An example of tetrachoric contingency table is presented in Table 2 for the Torino radar; it refers to radar echoes aloft for a single polar bin (average area within the radar umbrella of approximately 0.1 km^2). If we average more radar bins (0.25 km^2 area), the wet-dry discrimination slightly increases: the number of missing detection decreases from 6 to 5 (146 hits); similar results are obtained by averaging a number of radar bins 4 times larger (1 km^2 area). Note that the radar and gauge thresholds are different as consequence of the overall radar underestimation (see next Section 2.3.2 for details).

	G ≥ 0.5 mm/day	G < 0.5 mm/day	
R ≥ 0.2 mm/h	145	4	149
R < 0.2 mm/h	6	13	19
	151	17	**168**

Table 2: Contingency table between the Torino radar bins (average area ~0.1 km^2) and the **6** Weather Underground rain gauge values during **28** rainy days in April and May 2013.

In this study we will use two scores that can be applied to both tetrachoric and polychoric tables:
- the Heidke Skill Score (HSS), also known as Kappa Index of Agreement (KIA), Khat, …
- the Hanssen-Kuipers (HK) score also known as True Skill Score (TSS), …

Details regarding these two scores can be found in literature; the interested reader may refer, among others, to the paper by *Tartaglione* [2010] regarding HK and to the work by *Hogan* et al. [2009] regarding HSS. In particular, the Appendix of this last paper interestingly aims at estimating confidence intervals in the HSS.
Table 3 shows the values of the scores as a function of the radar area used (around the gauge): by averaging a larger number of radar echoes, the agreement seem to improve. An even larger improvement is observed in Israel by increasing the number of radar bins used in the average calculus. (see Table 3.4.1).

TO radar (Italy): daily wet-dry discrimination as a function of the radar AREAL integral	0.1 km^2	0.25 km^2	1 km^2
Heidke Skill Score (HSS)	0.689	0.713	0.713
Hanssen-Kuipers (HK) score	0.725	0.732	0.732

Table 3.3.1: Daily wet versus dry discrimination for the Torino radar as a function of the radar area used around the gauge to derive the daily (average) precipitation amount at the ground.

3.3.2 Agreement between gauge and radar-derived daily precipitation amounts

Table 3.3.2a and Table 3.3.2b show quantitative assessment of the radar-gauge agreement in terms of mean error (Bias in dB) and dispersion of the error around the mean (Scatter in dB). For both scores, there is a dependency on the size of the area of the radar-target-region around the gauge used to estimate the radar-derived daily amount. However, while the maximum difference in bias is ~0.15 dB, the maximum difference in scatter is even 0.26 dB. As expected, the performances are counterbalanced: an improvement in the value of the scatter corresponds to a poorer bias. It is also interesting to note that the number of wet-wet daily amounts is 145 when the area of the radar-target-region around the gauge is 0.1 km^2, while it is 146 when such area is increased to 0.25 or 1 km^2.
A larger area of the radar-target-region causes not only a better performance in terms of scatter (in dB) but also a better correlation coefficient between (linear) radar-derived and gauge-observed daily amounts (see last line of Table 3.3.2b). Consequently we conclude the following:
- a 1 km^2 radar-target-region around the rain gauge seems to be optimal: it performs better than 0.25 km^2, which in turns it is better than a smaller one (0,1 km^2)

TO radar (Italy): average error	Number of radar-gauge couples	0.1 km²	0.25 km²	1 km²
Overall BIAS in dB	168; 168; 168	-0.67 dB	-0.72 dB	-0.82 dB
Conditional (wet-wet) BIAS in dB	145; 146; 146	-0.69 dB	-0.74 dB	-0.84 dB

Table 3.3.2a: Daily mean field bias for the Torino radar as a function of the radar area used to derive the remotely sensed precipitation estimate at the gauge "point" site.

TO radar (Italy): dispersion of the error around the mean	Degrees of Freedom	0.1 km²	0.25 km²	1 km²
Scatter in dB	143; 144; 144	1.94 dB	1.93 dB	1.68 dB
Explained variance in percentage	143; 144; 144	56.3%	58.8%	61.4%

Table 3.3.2b: Agreement between (wet-wet) radar-gauge daily amounts in terms of scatter in dB and square of the correlation coefficient multiplied by 100. Torino radar and six rain gauges under its surveillance area.

Fig. 1 shows the daily radar-gauge scatter plot for the case of 1 km^2 radar-target-region: as it can be seen from Tables 3.3.2 a) and b), the number of wet-wet radar-gauge couples is 146; (conditional) bias and scatter computed from such samples results to be -0.84 dB and 1.68 dB, respectively.

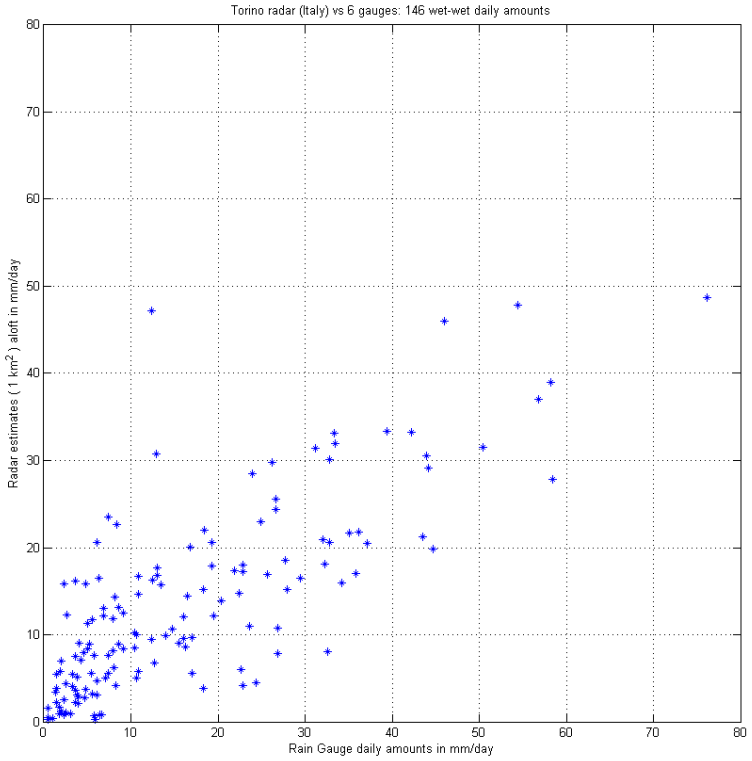

Fig. 1: Scatter plot of radar vs gauge daily amounts for the Torino radar: April-May 2013.

3.4 QPE performances for the Gilat radar (Israel): winter 2013

The 2nd low-cost radar analyzed in this study is located in southern Israel inside the Gilat Research Center (Agricultural Research Organization). In this region, the rain rate and the average annual rainfall have a steep, downward gradient from North to South and from West to East. In general, rain events are stronger and wider at sea (western Israel) and become weaker and rarer during their movement toward the south-eastern part of Israel (Goldreich, 2003). At Gilat longitude (34°.66), the mean annual precipitation ranges from approximately 400 mm in the north to 200 mm in the south; at Gilat latitude (31°.33) it ranges from 474 mm in the west to 240 mm in the east.

For the quantitative evaluation of the radar estimates we have been using **twelve** rain gauges of the Israeli national weather service: their average (±standard deviation) range from the radar site is 19.4±7.1 km; minimum (maximum) range is 6 (28.2) km. During winter 2013 there were **20** rainy days. Out of the available **240** daily amounts, 180 were classified as wet according to gauges (G>0.5 mm/day), while 185 were classified as wet (R>0.2 mm/day) according to the radar (0.1 km^2 radar-target-regions). Among them, in 162 cases both the radar estimate and corresponding gauge measurement at the ground agree in classifying the radar-gauge couple as "wet", hence indicating a rather intermittent rain situation. The conditional average daily precipitation based on such 162 wet-wet radar-gauge couple is (4.7) 10.1 mm according to (radar) gauges (0.1 km^2 radar-target-regions), which corresponds to an "overall Bias" of –3.29 dB (radar underestimation, see also Table 3.4.2a). The corresponding Coefficient of Variation (relative dispersion) is 1.16 (1.39) mm according to gauges (radar).

3.4.1 Radar-based wet vs dry discrimination (in rainy days) using the gauge as reference

The wet versus dry discrimination in Israel is much less successful than in Torino: as shown in Table 3.4.1 both HSS and HK are of the order of 0.5, while in Torino they were around 0.7 (see Table 3.3.1); there is another significant difference, compared to the southern side of the Western Alps: while for the Torino radar, the performances of the wet-dry discrimination were more or less equal at the three radar spatial scale used for deriving average daily amounts, for the Israeli radar the performances improve for larger areas (see e.g. 2nd and last column of Table 3.4.1)

Gilat radar (Israel): daily wet-dry discrimination as a function of the radar AREAL integral	0.1 km^2	0.25 km^2	1 km^2
Heidke Skill Score (HSS)	0.498	0.511	0.579
Hanssen-Kuipers (HK) score	0.482	0.493	0.567

Table 3.4.1: Daily wet versus dry discrimination for the Gilat radar as a function of the radar area used around the gauge to derive the daily (average) precipitation amount at the ground.

3.4.2 Agreement between gauge and radar-derived daily precipitation amounts

As expected, also the agreement between rainy amounts is much less successful in Israel than in Torino. Performances are poorer both in terms of mean error (Bias in dB, see Table 3.4.2a) and dispersion of the error around the mean (Scatter in dB, see Table 3.4.2b).
The (mean field) Bias is even smaller than -3 dB (less than 50% of the precipitation is estimated by the radar); as in Torino, the overall ratio between radar-total and gauge-total is a robust and resistant parameter, not too sensitive to the three radar spatial scale used nor to the thresholds used for discriminating between a wet versus a dry day (0.5 mm/day for the gauge, 0.2 mm/day for the radar; different thresholds as a consequence of the overall radar underestimation).

Gilat radar (Israel): average error	Number of radar-gauge couples	0.1 km^2	0.25 km^2	1 km^2
Overall BIAS in dB	235; 239; 242	-3.30 dB	-3.17 dB	-3.19 dB
Conditional (wet-wet) BIAS in dB	162; 162; 163	-3.29 dB	-3.18 dB	-3.20 dB

Table 3.4.2a: Daily mean field bias for the Gilat radar as a function of the radar area used around the gauge to derive the remotely sensed precipitation estimate.

Gilat radar (Israel): dispersion of the error around the mean	Degrees of Freedom	0.1 km^2	0.25 km^2	1 km^2
Scatter in dB	160; 160; 161	3.55 dB	3.57 dB	3.53 dB
Explained variance in percentage	160; 160; 161	35.0%	36.4%	36.7%

Table 3.4.2b: Agreement between (wet-wet) radar-gauge daily amounts in terms of scatter in dB and square of the correlation coefficient multiplied by 100. Gilat radar and 12 rain gauges under its surveillance area.

The Scatter is also much worse than in Torino; for the Gilat radar, it is as large as 3.57 dB (worst case, not too different from the 3.53 dB, which is the best case). In Torino, performances are much better, probably also due to the more stratiform nature of the analyzed events.

There are other significant differences compared to the case of the Torino radar: for instance, the scatter shows little dependence on the size of the area of the radar-target-region around the gauge used to estimate the radar-derived daily amount: for the Torino radar, the worst-best case difference is as large as 0.26 dB; for the Gilat radar, it is as small as 0.04 dB.
Another (somehow surprising) difference is that the bias does not get worse by increasing the size of the radar-target-region around the gauge. All considered (bias, scatter and correlation), we come to the same conclusion obtained to the southern side of the Western Alps:

- a 1 km^2 radar-target-region around the rain gauge seems to be optimal.

Fig. 2 shows the daily radar-gauge scatter plot for the case of 1 km^2 radar-target-region: as it can be seen from Tables 3.4.2 a) and b), the number of wet-wet radar-gauge couples is 160; (conditional) bias and scatter computed from such samples results to be -3.20 dB and 3.53 dB, respectively.

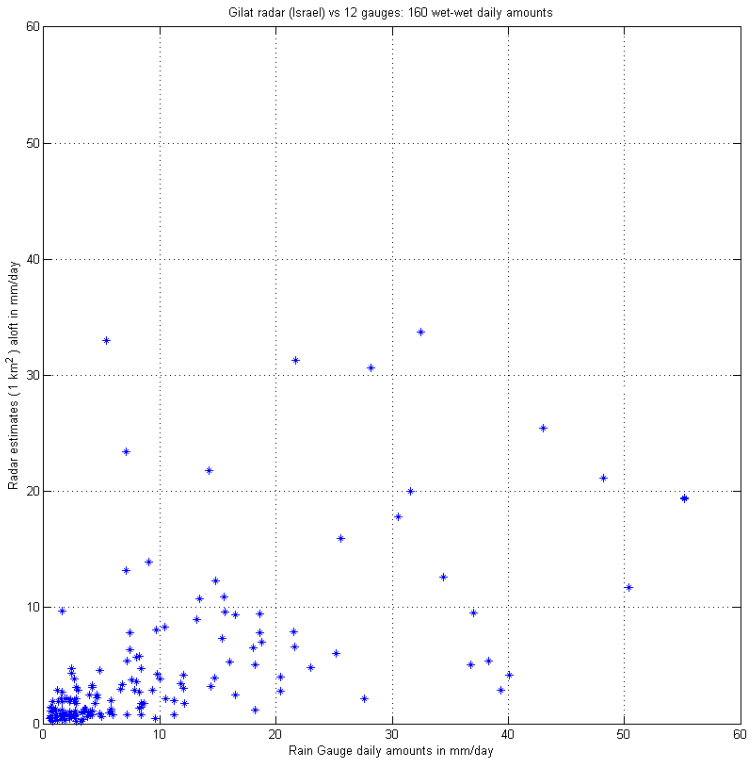

Fig. 2: Scatter plot of radar vs gauge daily amounts for the Gilat radar: winter 2013.

Why Gilat radar performances are considerably worse than Torino radar? (We will see in Section 4 that Torino radar performances are particularly good, in the sense that they are even in line with three-dimensional (3D) vertical reflectivity profile corrected radar estimates retrieved with operational MeteoSwiss C-band radars …) We see three possible causes (eventually combined together): worse radar quality; worse gauge quality; larger variability of the precipitation field in semi-arid climate and consequently larger intrinsic disagreement in the different radar-gauge sampling modes.

4 QPE benchmark (Vertical Reflectivity Profile corrected C-band radars)

The following Section 4.1 provides a benchmark for “wet-wet” performances of the Torino and Gilat radar; it is based on rain gauges, which are located at close ranges of three C-band radars belonging to the Swiss weather radar network. In general, we expect better performances from the C-band network because of the more sophisticated and appropriate system design (3D complex orography tailored scan program;) and innovative solutions for compensating shielding of the radar beam by the mountains (including mesobeta Vertical Reflectivity Profile corrections; for more details see *Germann and Joss* [2002]). A detailed description of the Swiss solution can be found in *Germann et al.* [2006]. Also, we expect better performance

at C-band because of less attenuation (including wet-radome attenuation). Another advantage is the better angular resolution: as seen in Sec. 3.2, for instance, at the average gauges distance, the Monte Lema radar sampling volume is ten times smaller!

4.1 Agreement between gauge and radar-derived daily precipitation amounts (May-June 2013)

4.1.1 Monte Lema radar (southern side of the Western Alps) and 4 nearby rain gauges

The Monte Lema radar is located at 1625 m above sea level, just in front of the Verbano lake and not far from Lugano; its latitude is 46°.0418; the longitude is 8°.8344.
For the quantitative evaluation of the radar estimates we have been using 4 rain gauges (MAG, OTL, LUG, SBO) of the MeteoSwiss network; their average(±standard deviation) range from the radar site is 15.8±5.3 km and they are located at much smaller altitude (299±76 m above sea level).
During the 61 days of May-June 2013, there are 96 wet-wet radar-gauge couples (out of a total of 244 possible cases); during such days, the average daily precipitation is 14.4 (12.6) mm according to gauges (radar), which corresponds to a conditional (wet-wet) Bias of -0.6 dB (see also Table 4.1.1a).
The corresponding Coefficient of Variation is 1.07 (0.88) mm according to gauges (radar).
Fig. 3 shows the daily radar-gauge scatter plot for the case of 1 km^2 radar-target-region: as it can be seen from Tables 4.1.1 a) and b), the number of radar-gauge couples is 96; (conditional) bias and scatter computed from such samples results to be -0.60 dB and 1.93 dB, respectively.

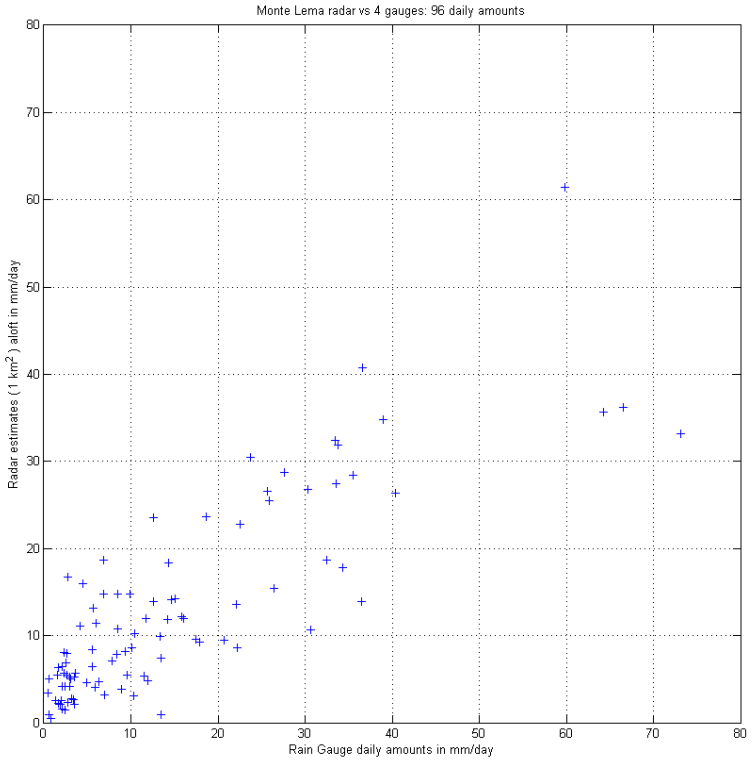

Fig. 3: Scatter plot of radar vs gauge daily amounts for the Swiss Lema radar: May-June 2013.

Table 4.1.1a and Table 4.1.1b show quantitative assessment of the radar-gauge agreement in terms of mean error (Bias in dB) and dispersion of the error around the mean (Scatter in dB). Not surprisingly, results are similar to what obtained in Torino, which is also located in the southern side of the western Alps. For both scores, there is a light dependency on the size of the area of the radar-target-region around the gauge: the difference in bias (scatter) is -0.08 (+0.09) dB. As expected, the performances are counterbalanced: an

improvement in the value of the bias corresponds to a poorer scatter. All considered, we come to the same conclusion previously obtained not only to the southern side of the Western Alps, but also in Israel:

- a 1 km^2 radar-target-region around the rain gauge seems to be optimal.

Lema C-band radar (CH): average error	Number of radar-gauge couples	1 km²	25 km²
Conditional (wet-wet) BIAS in dB	96; 96	-0.60 dB	-0.52 dB

Table 4.1.1a: Daily mean field bias for the Monte Lema radar as a function of the radar area used to derive the remotely sensed precipitation estimate at the gauge "point" site.

Lema C-band radar (CH): dispersion of the error around the mean	Degrees of Freedom	1 km²	25 km²
Scatter in dB	84; 84	1.93 dB	2.02 dB
Explained variance in percentage	84; 84	70.5%	69.5%

Table 4.1.1b: Agreement between (wet-wet) radar-gauge daily amounts in terms of scatter in dB. Monte Lema radar and four rain gauges under its surveillance area.

4.1.2 La Dole radar (western side of the Western Alps) and 3 nearby rain gauges

The Dole radar is located at 1680 m above sea level, just in front of the Lemano lake and not far from Geneva; its latitude is 45°.4262; the longitude is 6°.1002.
For the quantitative evaluation of the radar estimates we have been using 3 rain gauges (CGI, GVE, PUY) belonging to the MeteoSwiss automatic network; their average(±standard deviation) range from the radar site is 25.1±17.6 km and they are located at much smaller altitude (444±21 m above sea level).
During the 61 days of May-June 2013, there are 86 wet-wet radar-gauge couples (out of a total of 183 possible cases); during such days, the average daily precipitation is 7.3 (6.0) mm according to gauges (radar), which corresponds to a conditional (wet-wet) Bias of -0.8 dB (see also Table 4.1.2a). The corresponding Coefficient of Variation is 0.90 (0.91) mm according to gauges (radar).
Fig. 4 shows the daily radar-gauge scatter plot for the case of 1 km^2 radar-target-region.

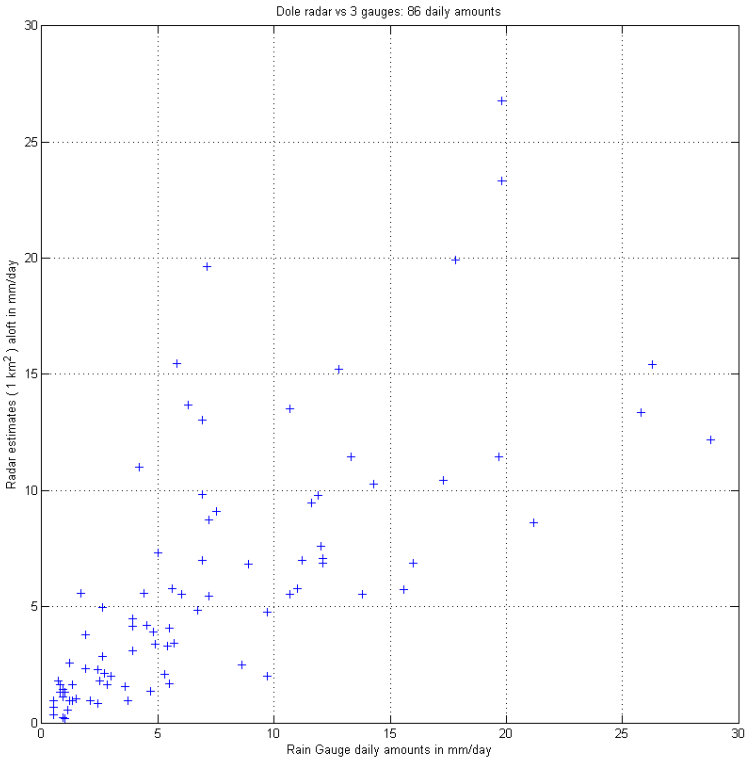

Fig. 4: Scatter plot of radar vs gauge daily amounts for the Swiss Dole radar: May-June 2013.

As it can be seen from Tables 4.1.1 a) and b), the number of radar-gauge couples is 86; (conditional) bias and scatter computed from such samples results to be -0.82 dB and 1.93 dB, respectively.
Table 4.1.2a and Table 4.1.2b show quantitative assessment of the radar-gauge agreement in terms of mean error (Bias in dB) and dispersion of the error around the mean (Scatter in dB). For this radar, there is practically no dependency on the size of the area of the radar-target-region around the gauge: the difference in bias (scatter) is 0.00 (-0.05) dB. Hence, for the La Dole radar the 25 km^2 radar-target-region seems to perform in a similar way to the 1 km^2 radar-target-region; this fact is confirmed by the explained variance (last line in Table 4.1.2b).

La Dole C-band radar (CH): average error	Number of radar-gauge couples	1 km^2	25 km^2
Conditional (wet-wet) BIAS in dB	86; 86	-0.82 dB	-0.82 dB

Table 4.1.2a: Same as Table 4.1.1a but for the Dole radar.

La Dole C-band radar (CH): dispersion of the error around the mean	Degrees of Freedom	1 km^2	25 km^2
Scatter in dB	84; 84	2.35 dB	2.30 dB
Explained variance in percentage	84; 84	51.2%	49.3%

Table 4.1.2b: Same as Table 4.1.1b but for the Dole radar and three nearby rain gauges.

4.1.3 Albis radar (northern side of the Western Alps) and 8 nearby rain gauges

The Albis radar is located at 930 m above sea level on a hill not far from Zurich; its latitude is 47°.2854, its longitude is 8°.5130.
For the quantitative evaluation of the radar estimates we have been using 8 rain gauges (BEZ, BUS, KLO REH, SHA, SMA, TAW, WAE) belonging to the MeteoSwiss automatic network; their average (±standard deviation) range from the radar site is 27.2±12.9 km and they are located at smaller altitude (450±76 m above sea level).
During the 61 days of May-June 2013, there are 264 wet-wet radar-gauge couples (out of a total of 488 possible cases); during such days, the average daily precipitation is 7.0 (5.5) mm according to gauges (radar), which corresponds to a conditional (wet-wet) Bias of -1.0 dB (see also Table 4.1.3a).
The corresponding Coefficient of Variation is 1.23 (1.13) mm according to gauges (radar).
Fig. 5 shows the daily radar-gauge scatter plot for the case of 1 km^2 radar-target-region: as it can be seen from Tables 4.1.3 a) and b), the number of radar-gauge couples is 246; (conditional) bias and scatter computed from such samples results to be -1.02 dB and 1.35 dB, respectively.
Table 4.1.3a and Table 4.1.3b show quantitative assessment of the radar-gauge agreement in terms of mean error (Bias in dB) and dispersion of the error around the mean (Scatter in dB). For both scores, there is a light dependency on the size of the area of the radar-target-region around the gauge: the difference in bias (scatter) is -0.06 (-0.04) dB. It is somehow surprising that performances are not counterbalanced: both bias scatter show an improvement; the explained variance is almost equal. Hence, a 25 km^2 radar-target-region seems to be slightly better than 1 km^2 for the Albis radar.

Albis C-band radar (CH): average error	Number of radar-gauge couples	1 km^2	25 km^2
Conditional (wet-wet) BIAS in dB	264; 264	-1.02 dB	-0.96 dB

Table 4.1.3a: Same as Table 4.1.1a but for the Albis radar (0.7 dB Calibration Unit compensation).

Albis C-band radar (CH): dispersion of the error around the mean	Degrees of Freedom	1 km^2	25 km^2
Scatter in dB	262; 262	1.35 dB	1.31 dB
Explained variance in percentage	262; 262	84.2%	84.1%

Table 4.1.3b: Same as Table 4.1.1b but for the Albis radar and eight nearby rain gauges.

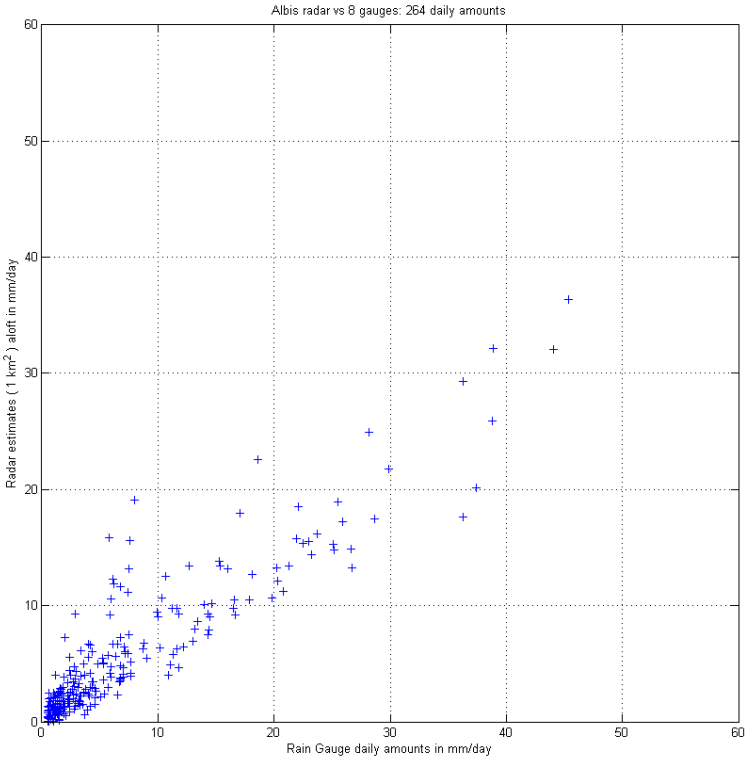

Fig. 5: Scatter plot of radar vs gauge daily amounts for the Swiss Albis radar: May-June 2013.

Albis C-band radar (CH): dispersion of the error around the mean	Degrees of Freedom	1 km²	25 km²
Scatter in dB	262; 262	1.35 dB	1.31 dB
Explained variance in percentage	262; 262	84.2%	84.1%

Table 4.1.3b: Same as Table 4.1.1b but for the Albis radar and eight nearby rain gauges.

5 Polarimetric, Doppler, mobile, X-band radar: advanced meteorological and atmospheric observations

State-of-the-art precision approach radars (PARs) recently acquired by the Swiss Confederation do have weather induced performance limitations that are mainly caused by precipitation and wind shearing within the radars cell. In order to quantify these effects at the Swiss airport sites where the radars are going to be installed, a sophisticated, meteorological, polarimetric, mobile, Doppler X-band radar has been acquired. The products generated by the weather radar shall be used to assess the state of the atmosphere within and around the PAR cells, such that the effect of wind shearing and precipitation on the PAR performance can be assessed. MeteoSwiss is currently operating the X-band radar in parallel to the PAR site acceptance tests at the designated locations. Tools are under development such that the rain rate and the wind shearing can be deduced from the polarimetric and Doppler moments with sufficient accuracy.

This Section 5 presents preliminary results obtained with such innovative X-band radar system. Its cost is roughly one order of magnitude larger than the simple and minimalistic mini radar presented in Sec. 3; not surprisingly, the list of benefits associated to this system is long and the spectrum of possible meteorological and atmospheric observations is wide.

Obviously, the system has much better performances in terms of sensitivity, mainly because of

- the presence of a high quality Low Noise Amplifier at the first stage of the receiver chain.
- A larger, more directive antenna (HPBW=1.3° instead of 3.6°), which implies much better resolution.
- A more powerful magnetron (70 kW instead of 10 kW Tx peak power).

All considered, this system is more than **20 dB better** in **sensitivity** than the low-cost radar described in Section 3. It is sensitive enough to detect the power emitted by the Sun; the Sun signal can be used for monitoring the Rx chain, assess electromagnetic beam pointing and, with additional efforts, relative and (quasi-)absolute calibration of the receiver chain.

Another remarkable advantage consists in its ability of retrieving the **Doppler** component: this magnetron system is in fact coherent on reception. Its Doppler capabilities offer great advantages not only for advanced meteorological and surveillance observations but also for ground clutter rejection. It is worth noting the system provides not only the 1st (mean radial velocity) and 2nd (spectral width) Doppler moment, but also the whole spectrum, i.e. the received signal power as a function of the Doppler velocity.

Furthermore, being **on wheel**, the system can be easily moved and deployed in any part of the country; it has also powerful and **precise 3D scanning capabilities**.

Last but not least, this high-performance radar determines the standard dual-polarization meteorological quantities (Z_{DR}, Φ_{dp}, and ρ_{HV}) from simultaneous horizontal (H) and vertical (V) transmissions. The return signals are measured in two parallel H and V receiving channels. Because the parameters are determined from simultaneous measurements they are not affected by Doppler phase shifts that increase the variance of Φ_{dp}, and ρ_{HV} when alternating H and V polarizations are transmitted. The approach has the additional advantage that a high-power polarization switch is not needed. According to measurements performed at the Site Acceptance Test (*Hueppi et al.* [2012]), the radar operates on a peculiar hybrid approach in which H and V signals are transmitted simultaneously, in this case in the form of circular polarization, and are received in parallel H and V channels. The transmitted and received signals are in different polarization bases, such that the received signals are both copolar-like. The advantage of transmitting and receiving H and V polarizations simultaneously is that Z_{DR}, Φ_{dp}, and ρ_{HV} are determined directly from the same transmitted pulse, which is, at zero lag, and are not contaminated by Doppler effects. Also, a polarization switch is not needed. Dual receiving channels are required, but modern receiving techniques enable these to be implemented in a highly matched manner. In the rest of the Section we will use the acronym DXCH for this system (D reminds us its Doppler and dual-pol capabilities, X for the band, CH reminds us that it belongs to the Swiss Confederation).

5.1 Measurements field experiments and DXCH radar sites

Up to now, the DXCH has been deployed in three different sites:

- the narrow and deep Hasli valley (see Sec. 5.2) at the Meiringen site (from May to July 2013);
- the Magadino plain, which lies (see Sec. 5.3) between the Verbano lake (West) and Bellinzona town (East) along the last Swiss part of the Ticino river (from September 2012 to April 2013);
- the hilly areas around Payerne (Sec. 5.4) in the Swiss plateau (from September 2013 up to now).

5.2 Innovative scan program: monitoring the atmosphere in co-located PAR cells

In addition to the conventional “azimuthal” volume scan program tailored to the Swiss Alps (*Rad4Alp* MeteoSwiss Specification and Request for Proposal [2009]), the DXCH is programmed to run volumetric scan tailored to the PAR systems in the elevation plane (see Fig. 6, next page). It consists of a series of 13 Range Height Indicator (RHI) images in in the main airplane approach direction (up to $\pm 12°$ with respect to the main approach direction in the azimuthal plane, see Fig. 6.a); seven (six) RHI scans are characterized by an upward (downward) moving antenna having a radial constant velocity of 8°/s in the Elevation plane within the range delimited by angles of elevation set to +2° and +30°, respectively.

A detailed sketch of this optimized scan (PAR sector scan) in the Elevation plane can be found in Figure 6.b. In the subsequent data processing, the individual RHI scans are compiled into a single one according to the temporal and spatial proximity of the approaching aircraft. This means that from the ensemble of scans that are executed during the approach of the plane, the scans that optimally covered the trajectory of the approaching aircraft is selected and compiled into a single scan. An example is shown in Fig. 7. The antenna radial velocity of 10°/s together with an averaging angular width of 1° and an average PRF of 1750 Hz ensures high quality data: there are in fact 175 samples per individual processed angular interval.

The PAR sector scan program permits not only to monitor the weather along the airplane corridor, but also to assess the airplane Radar Cross Section (RCS) and polarimetric signature itself, by analyzing the DXCH echo exactly in the cell where the plane is rapidly passing by. An example of polarimetric signatures for the PC-12 airplane are listed in Table 5.1.

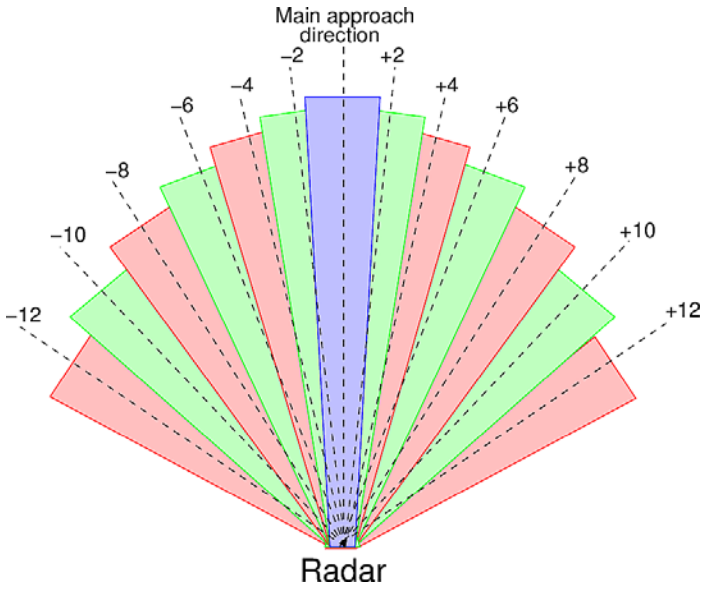

Fig. 6.a: Sketch of the innovative scan program tailored to the PAR system around the airplane main approach direction: schematic of the 13 interleaved RHI scans in the azimuthal plane (for the orthogonal plane, see Fig. 6.b).

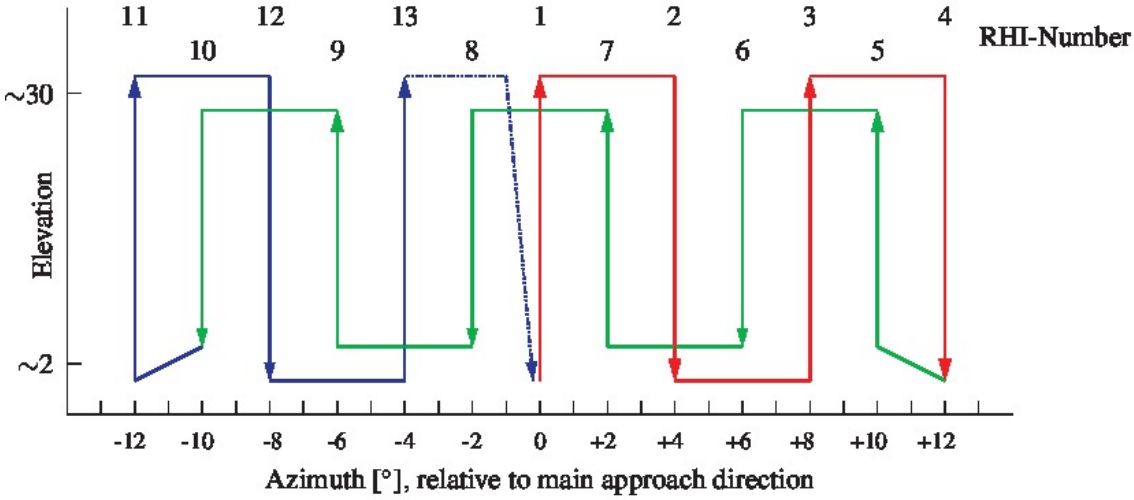

Fig. 6.b: Sketch of the PAR sector scan in the Elevation plane: the scan starts at the conventional reference point of 0°, which is chosen to be coincident with the airplane main approach direction.

Data have been acquired in rainy conditions on May 28, 2013 in the narrow and deep Hasli valley at the Meiringen site. Out of these five hits, the average Horizontal (Vertical) RCS results to be 3.8 (2.0) square meters, with a standard deviation of 2 m^2 for both polarizations. Despite different “aspects” associated with the various hits and “contamination” by rain, the observed RCS is relatively stable; this can probably be explained with the large number (175) of pulses involved in each measurement. It is worth noting that in the previous sentence, with the word “aspect” we mean not only the different aspect angles associated with each

pulse but also the fact that in every hit (average of ~175 pulses with different aspect angles) the airplane could be located at an azimuthal angular distance up to ±1° from the radar beam axis (see the 2° quantization in Azimuth clearly shown in Fig. 6.b). Regarding the airplane velocity and direction (in two cases the airplane was approaching, in 3 cases it was escaping, see column 8) we should not forget that the value in column 8 (Doppler effect) refer to its radial component, which is the actual velocity multiplied by the cosine of the angle between the radial and the airplane unit vectors … In cases where this angle were small, it could even happen the velocity to be folded. With the staggered PRF mode used (2000 and 1500 Hz), the unfolded velocity range is ±169.2 km/h.

The large number of averaged pulses should also be kept in mind when analyzing the real value of the complex copolar correlation coefficient at zero lag $\rho_{HV}(0)$ listed in column 7: 173 are the degrees of freedom associated to {HV*} observations involved in the estimate of $\rho_{HV}(0)$. Finally, in all five cases, the resulting Horizontal echo is stronger than the Vertical one (as can easily be seen in column 4).

Date	UTC time (seconds)	Horizontal reflectivity (dBZ)	Differential reflectivity (dB)	**Hor. RCS (m^2)**	**Ver. RCS (m^2)**	$\rho_{HV}(0)$	Doppler effect (m/s)	Range (m)
28.5.2013	30130	42.5	+6.4	**3.6**	**0.8**	0.32	+24.2	7107
28.5.2013	30248	28.0	+4.4	**0.6**	**0.2**	0.88	-12.3	15467
28.5.2013	33007	37.5	+2.2	**4.2**	**2.3**	0.46	+17.5	13698
28.5.2013	33083	42.0	+0.7	**6.0**	**5.2**	0.39	-11.5	9779
28.5.2013	33742	37.5	+1.8	**4.7**	**3.1**	0.82	+22.0	14495

Table 5.1: Airplane polarimetric signatures at X-band detected by the DXCH at the Meiringen airport.

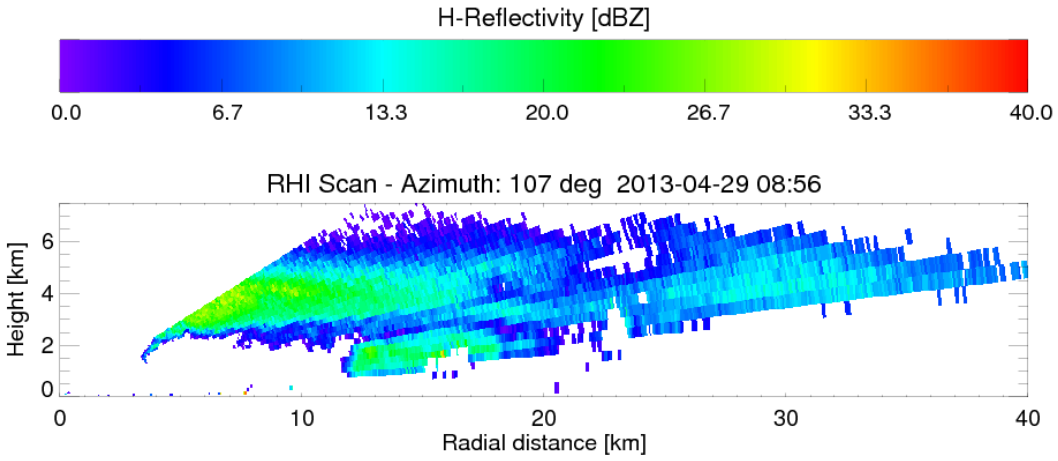

Fig. 7: Example of RHI scan along the main approach direction in Meiringen.

The Meiringen site, which is a narrow and deep valley surrounded by high mountains, is indeed a nightmare for siting a meteorological radar: on the one hand visibility is obviously extremely poor, on the other hand ground clutter strong. By way of example, the top pictures in fig. 8 show ground clutter characteristics in clear sky condition for an angle of Elevation of 2° when the radar is deployed down in the valley (altitude ~580 m): the left picture shows the 50 percentile (median), the right picture the 90 percentile. Similarly, the bottom pictures show same quantiles acquired in another clear sky day when the radar was deployed in a site located at higher altitude (~1270 m) on the South-oriented slope of the mountainous ridge that "follows" the Aare river on its right side. In this case, a blanking sector of almost 120° is necessary to avoid contamination (including multipath) by the nearby slopes. Note that in this case, radar reflectivity values have been converted in equivalent RCS values (simply by adding a "radar-dependent" constant plus 20 Log(range)).

The most used probability distribution functions (pdf) for ground clutter modeling are Rice, lognormal and Weibull (whose family includes the Rayleigh pdf). Obviously, they are asymmetric and skewed to the right.

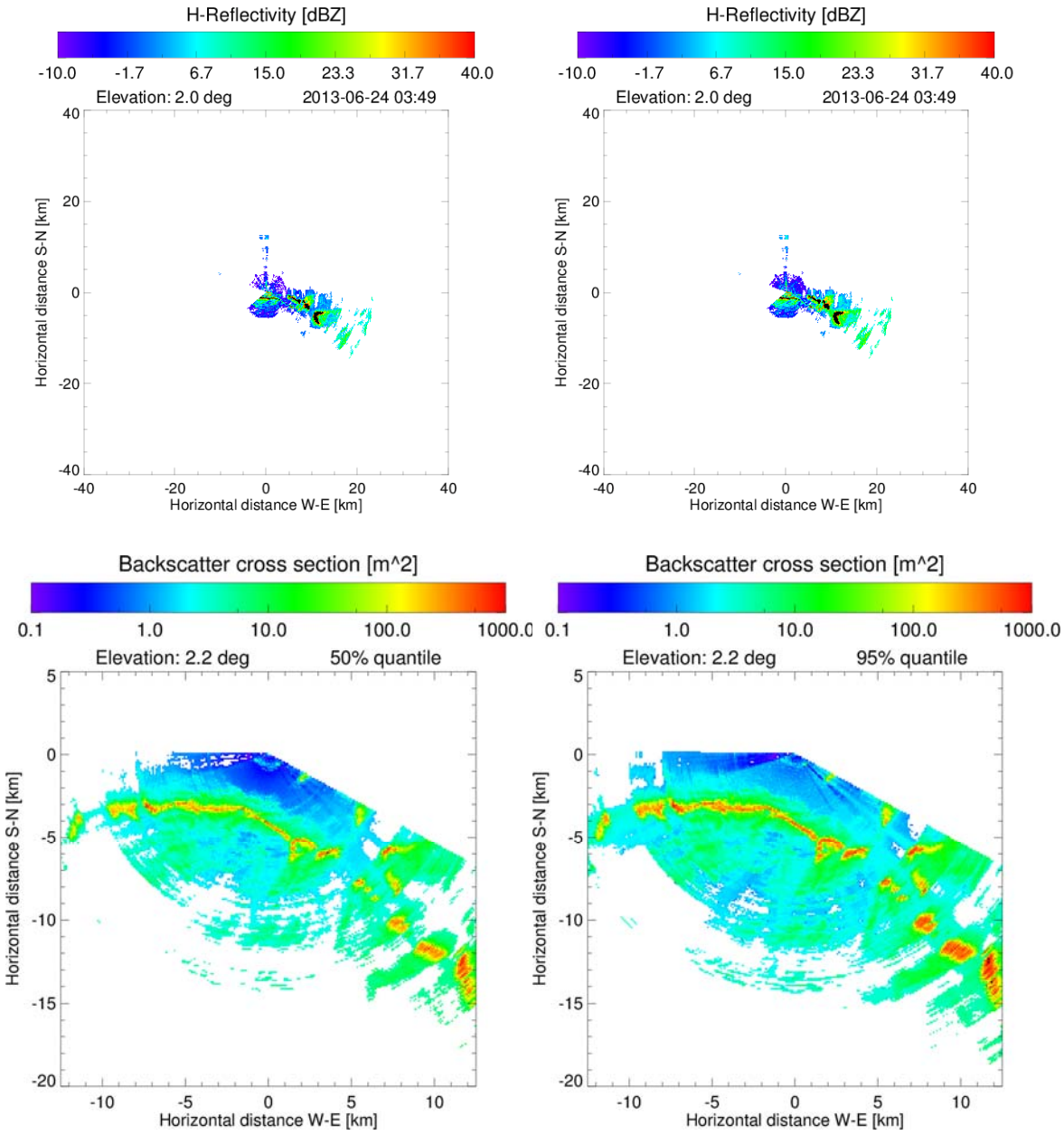

Fig. 8: median (left column) and 90 percentile (right column) of a series of ~100 PPI scans acquired in clear sky conditions in Meiringen (Horizontal channel). First line: site located down in the valley (580 m); Second line: site at higher altitude on the South-oriented slope of the mountainous ridge.

Consequently, the average RCS is always larger than the median; for Rayleigh, it is 1.6 dB; for Rice, it is between 0 dB and just less than 1.6 dB; for log-normal, is 0.115 times the square of the standard deviation in dB (see e.g., page 317 of *Joss et al.* [1974]).
An interesting property of the 90 percentile (Rayleigh, Weibull, “typical” lognormal pdf) is that it ranges 3-4 dB above the average RCS.

5.3 Measurements field experiments in Magadino

Also the Magadino site is by far not ideal for a weather radar. Nevertheless, it is still better than Meiringen.
Fig. 9 shows the Radar Cross Section of ground clutter echoes acquired with a single PPI in clear sky atmospheric conditions with an angle of Elevation set to 3.7° superimposed on a black-to-white (high-to-low altitude) digital terrain model (DTM). It is easy to recognize the shape of the northern part of the Verbano lake and various river valleys (e.g., from West to East, Maggia, Verzasca, Ticino, Moesa).

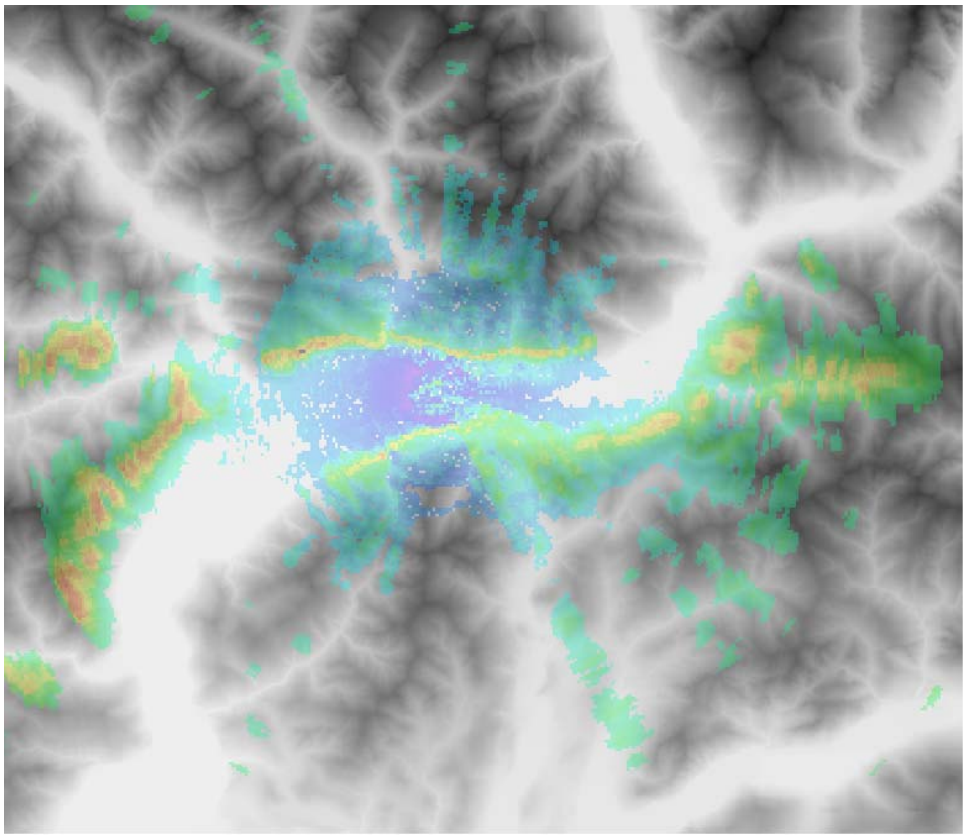

Fig. 9: An example of PPI backscatter cross section superimposed on a digital terrain model (Magadino site).

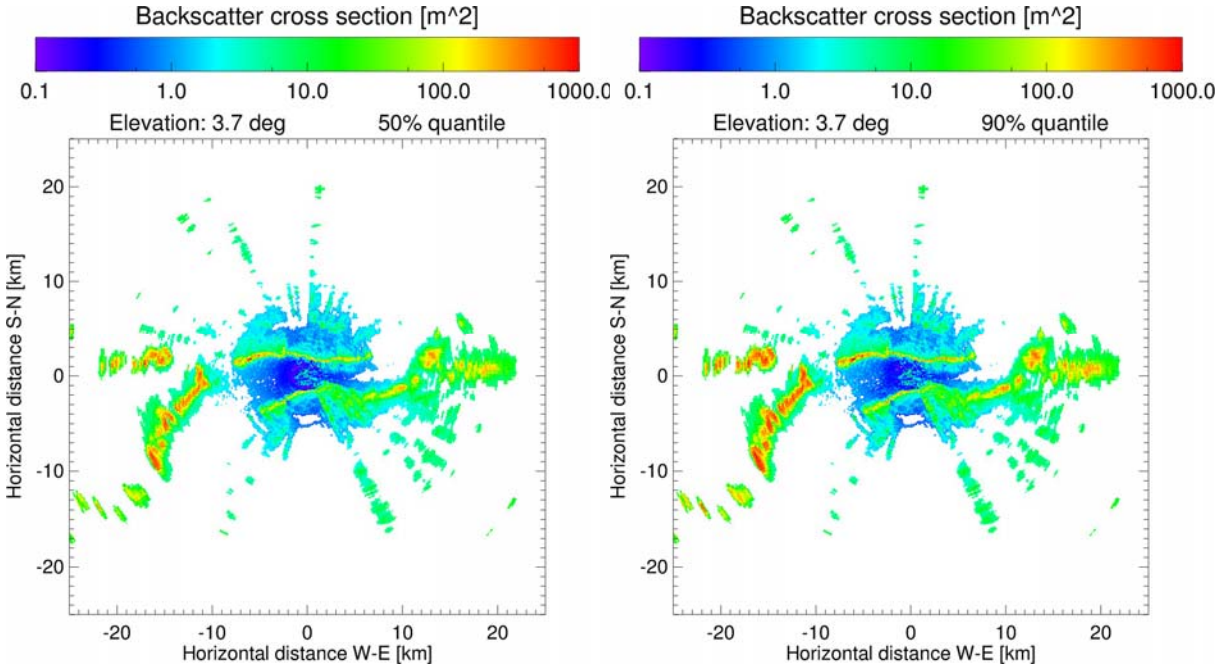

Fig. 10: median and 90 percentile of a series of 100 PPI scans acquired in clear sky (Horizontal channel).

The color palette for ground clutter echoes is the same as Fig. 10: from blu (low intensity) to red (high intensity) through cyan, green, yellow and orange (colors are matched on a log-transformed scale). Fig. 10 shows a statistical reduction of a large series of such PPI measurements (without orography). For each radar cell, all realizations are sorted and a given percentile is selected and displayed: the left picture shows the median (50%tile) RCS value, the right one the 90%tile. RCS values are expressed in square meters and have been derived from Horizontal reflectivity values in Z-units by combining the Probert-Jones weather

radar equation together with the point target radar equation. RCS values are log-transformed before color displaying: violet corresponds to -10 dB(m^2), while red to +30 10 dB(m^2). As expected, strongest echoes are found on the mountains slopes hit by the main lobe in areas characterized by smaller angle of incidence (see e.g. *Gabella and Perona* [1998]): it can be seen that the strong backscatter cross section values "follow" the shape of the orography (e.g. the Ghiridone and nearby mountains on the West); as expected, the Magadino plain (echoes from secondary lobes at grazing angles) is mostly violet/blu. Such plain, whose altitude is around 200 m above mean sea level, has a width in North-South direction of about 3 km and is surrounded by high mountain ranges in the North (up to 2400 m) and South (up to 2200 m) directions. Most ground clutter echoes have Doppler velocity close to zero, as can be seen in Fig. 11.
On the contrary, lake clutter echoes shows a much larger radial Doppler velocity so that the shape of the (northern part of the) Verbano lake can easily be distinguished both in the left (median) and right (90%tile) picture. For ground clutter rejection in the Magadino area, even a standard digital Fourier transform (DFT) filtering, which interpolate the power spectrum after having rejected a narrow band around 0 m/s with a predefined filter width, can be sufficient.

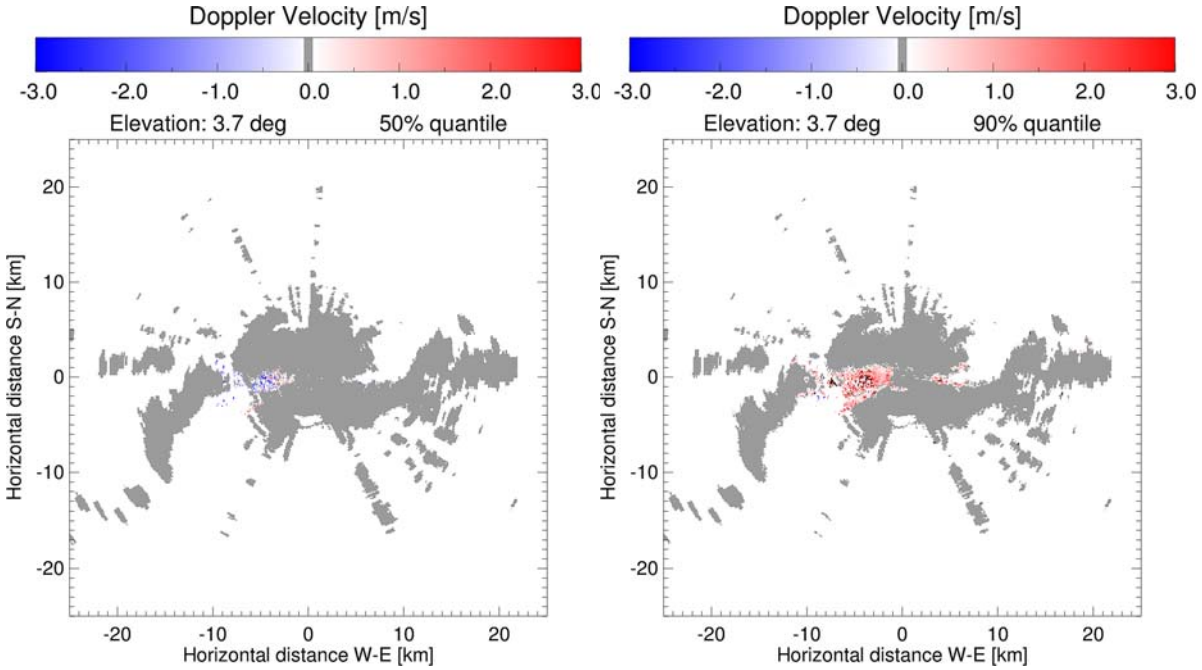

Fig. 11: Same as in Fig. 10 but for the Doppler velocity.

Fig. 12 clearly shows that the standard moving target indicator filter (MTI) implemented by the radar manufacturer, although not sufficient for a thorough clutter treatment (especially lake and forest clutter) is able to remove a significant amount of clutter without deleting the precipitation signal; obviously, care was taken in choosing the filter width (±0.34 m/s) so that precipitation signals with low radial velocities are not suppressed. By looking only at the left part of Fig. 12, it is not easy to guess how much energy is lost because of extinction by the radar beam while it propagates through the precipitation medium. The application of polarimetric information allows to overcome this problem, which is certainly dominant at the X-band attenuating wavelength: the estimate and correction of attenuation, hence justifying the added cost of matched and well calibrated dual receiving channels. In the examples shown in Figures 12 and 13, the ZPHI method developed by *Testud et al.* [2000] has been implemented. In Figure 12, the original PPI (left picture) and its corresponding attenuation corrected PPI scan (right picture) of the Horizontal reflectivity is shown. A clear effect of the correction procedure can be observed at and behind the intense rain cells.
As pointed out several time in the scientific literature, the evidence of attenuation can easily be seen in the image showing the original differential reflectivity, Z_{DR}, field (Fig. 13, left picture): behind strong cells the field exhibits negative values. At the given range (~12 km) and angle of Elevation (8.2°), the altitude of the radar beam axis is around 2000 m (see Fig. 14, 4th Elevation), which is smaller than the altitude of the 0° isotherm on that day (Sep. 25, 2012). Hence, we can exclude the presence of frozen vertically oriented hydrometeors.

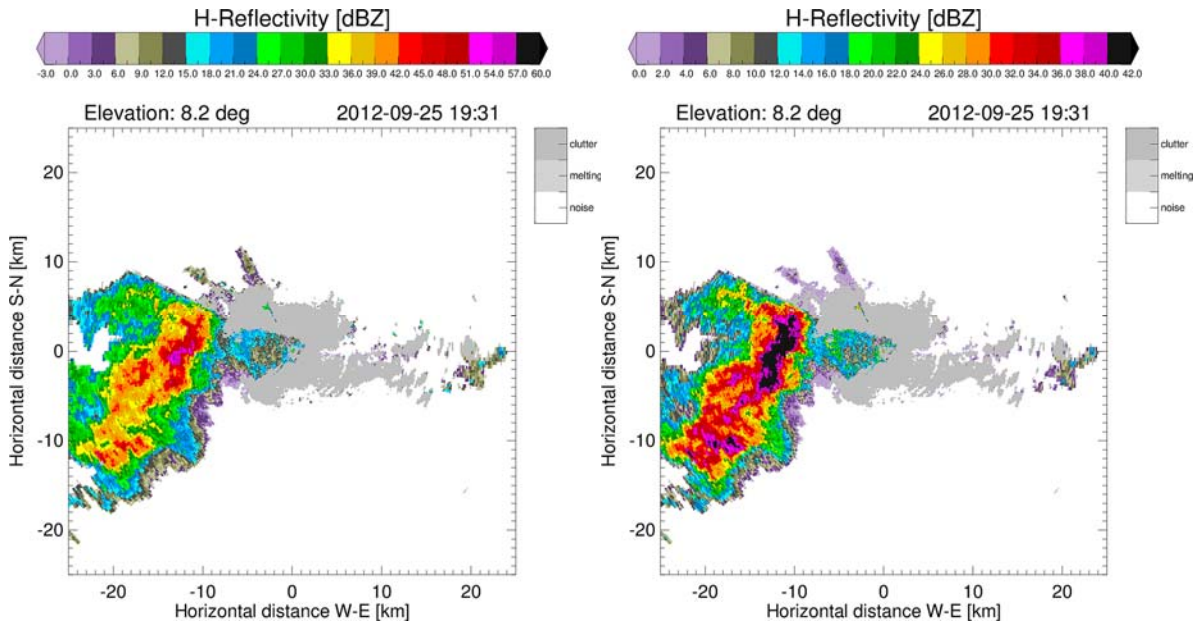

Fig. 12: Results of the so-called ZPHI method for correcting attenuation on the Horizontal reflectivity field; (left) original data, (right) attenuation-corrected data.

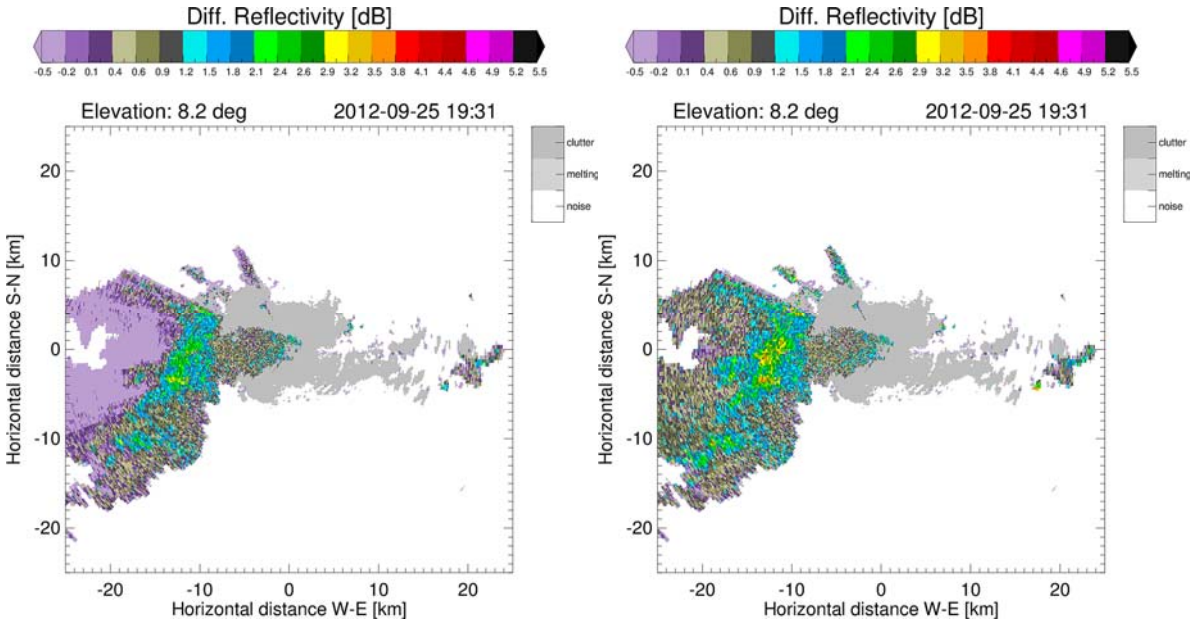

Fig. 13: Same as in Fig. 12 but for Z_{DR}; (left) original data, (right) attenuation-corrected data

Consequently, negative Z_{DR} values can only be explained assuming specific attenuation values at Horizontal polarization larger than those at Vertical polarization. From this viewpoint the ZPHI method seems to perform well: the attenuation corrected field (right picture in Fig. 13) exhibits similar, positive values both in front and behind the intense rain cells.

5.3.1 QPE intercomparison between C-band and X-band radar at the Magadino site

In this Sec. 5.3, we present a first comparison between C and X band radars with focus on very-high (quasi-equal) spatio-temporal resolution sampling volumes (~$7 \cdot 10^6$ m^3). The “Losone target area” is ~10 km west of the X-band radar; its visibility is good, since there are practically no significant obstacles along this west ray. Beyond the target area the ray hits the mountain behind Ascona-Losone at a range of approximately 13 km. The two lowest elevations of Monte Lema radar are instead partially blocked by the Gambarogno.

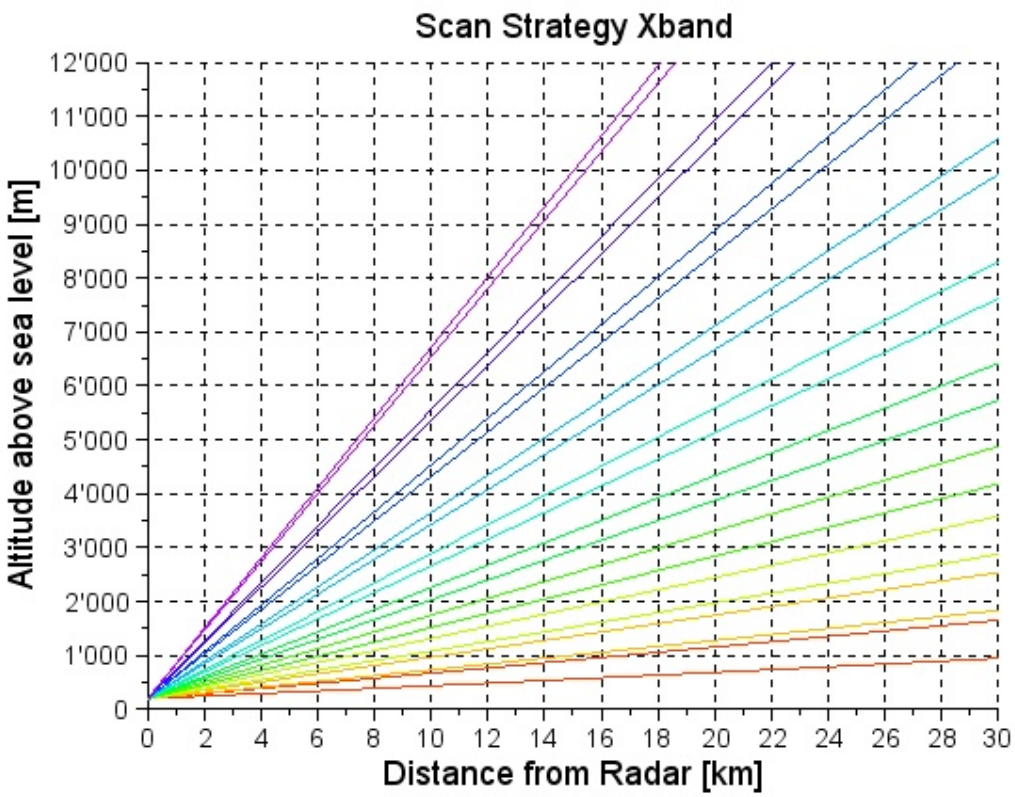

Fig. 14: Volume scan based on a series of 100 PPI Elevations in Magadino

Hence the comparison concerns echoes acquired with an angle of Elevation set to 1° for the C-band radar and 11.2° for the X-band; the altitude of the beam axis of the two radars is ~2 km. The event lasted 6 hours and took place on September 25, 2012 (see Figures 12 and 13). Six consecutive hourly rainfall amounts derived by averaging linear Z-values are shown in Table 5.3: columns 2 and 3 refer to the C-band radar, vertical and horizontal polarization; columns 4 and 5 refer both to X-band radar Horizontal polarization; column 4 shows original data, while in column 5 reflectivity data have been corrected for attenuation using the ZPHI method discussed in the previous Section.

	C-band radar		X-band radar	
UTC time	$R(\overline{Z}_V)$ mm/h	$R(\overline{Z})$ mm/h	$R(\overline{Z})$ mm/h	$R(\overline{Z}_{AC})$ mm/h
16-17	2.6	2.9	1.6	2.4
17-18	3.5	2.7	1.2	1.2
18-19	4.4	4.9	4.4	5.2
19-20	4.1	4.6	3.5	3.6
20-21	4.0	4.5	1.4	1.7
21-22	0.5	0.8	0.1	0.1

Table 5.3: Intercomparison between Monte Lema (C-band) and the X-band radar (Magadino site) on 25.9.2012.

Another comparison refer to November 11, 2012; obviously, the 0° isotherm was at smaller altitude. Consequently, we have opted for a target area without shielding nor blockage for Monte Lema radar: it is located above Locarno town (see Fig. 15). Its range is 5.8 km from the X-band radar in Magadino (average Azimuth is 264°) and 13.5 km from Monte Lema. The 1st elevation from Lema (-0.2°) is compared with the 5th elevation of the DXCH (11.2°): consequently the sampling volumes refer to an altitude of ~1500 m. Another advantage of this location is the presence of a rain gauge at our Institute (367 m altitude) as well as another gauge (203 m altitude) not far from the Magadino X-band radar.

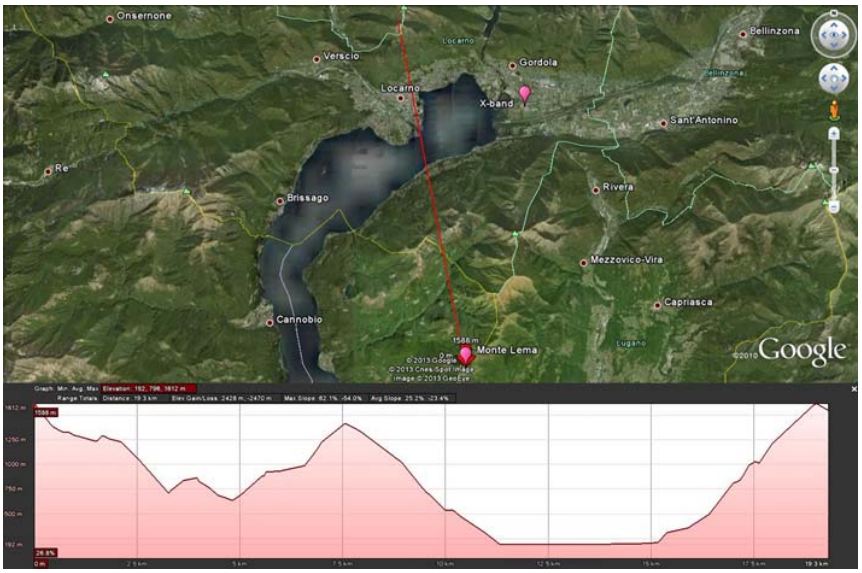

Fig. 15: The Locarno target area (N of the Lema C-band, W of the Magadino X-band)

Linearly averaged hourly reflectivities in dBZ show a reasonable agreement; an additional improvement is reached by correcting X- band values for attenuation (see Fig. 16, which displays log-transformed hourly averages: C-band on abscissa axis, X-band attenuation-corrected on ordinate axis). Despite attenuation-correction, the X-band underestimation is remarkably larger than the C-band one with respect to the Locarno Monti rain gauge. For the 17 rainy hours, the C-band Bias is -2.0 dB; the X-band Bias is -4.0 dB, which reduces to -3.6 dB in case of attenuation correction. Note that these values are not corrected with the mesobeta VRP, like it happens in the C-band operational product (see Section 4). Fig. 17 shows hourly rain rates for the 17 rainy hours on November 11, 2012 displayed on a Logarithmitic (decibel) scale. The blu line shows (tipping-bucket) rain gauge amounts recorded in Locarno Monti; the purple line shows rain amounts acquired by the gauge in Magadino. The difference in altitude between the two gauges is 164 m; their distance is 11.4 km. Not surprisingly, during such stratiform event in November, hourly amounts are quite similar: the Bias is 0.1 dB, the explained variance is 88% (as stated, we use Locarno Monti gauge as reference). The explained variance of C-band radar estimates is 66%; the corresponding one for X-band estimates is 51%, which increases to 65% in case of attenuation-corrected values

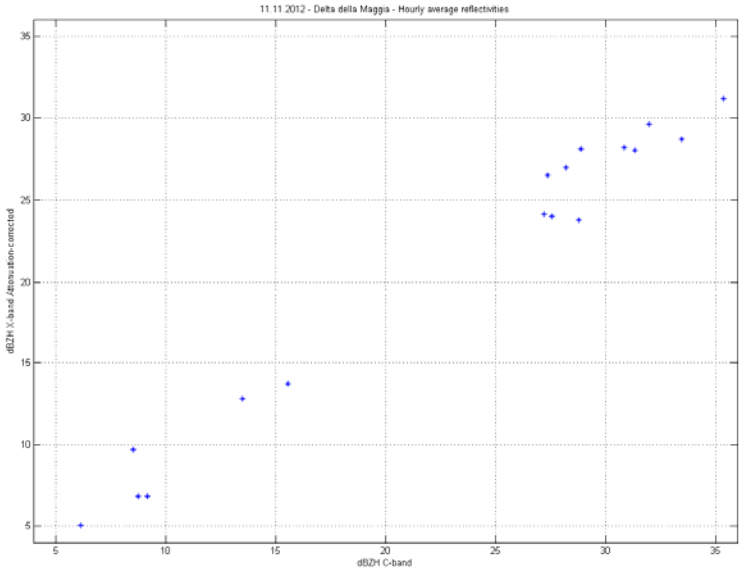

Fig. 16: C-band vs (attenuation-corrected) X-band hourly echoes on 11.11.2012.

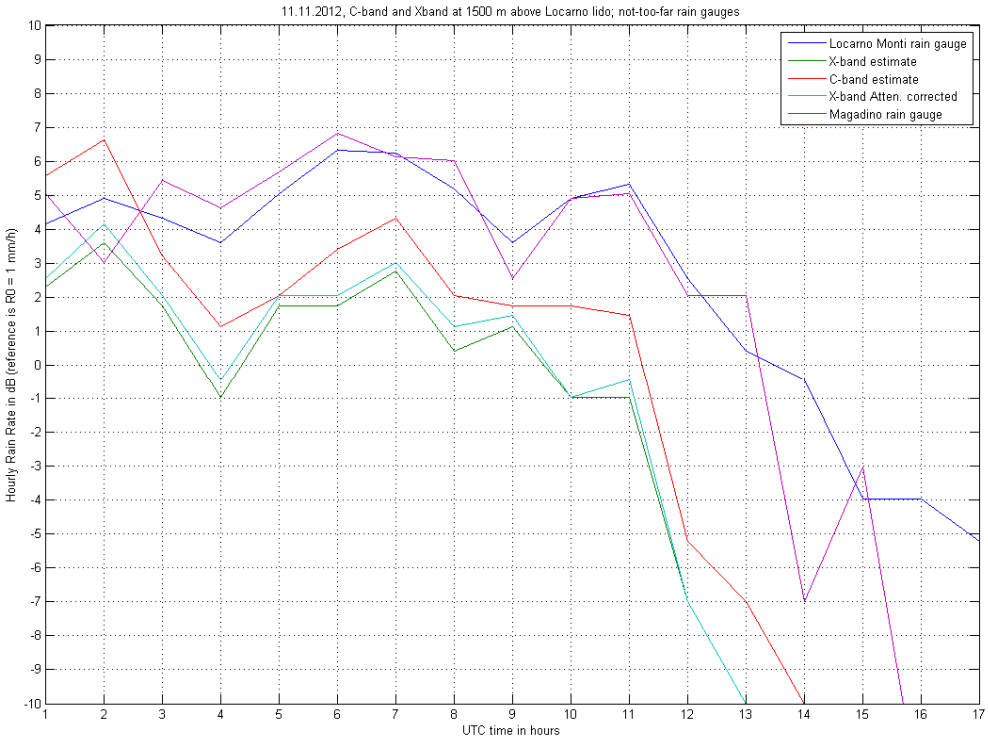

Fig. 17: C-band and X-band retrieved hourly rain rates on 11.11.2012 compared with nearby gauges.

5.4 Novel applications of radar Doppler spectra in Payerne

As stated in Sec. 5, one strong feature of the DXCH radar is its ability to provide and store for each 1°×75 m polar bin the whole spectrum, i.e. the received signal power as a function of the Doppler velocity. Hence, in addition to the mean Doppler velocity and its spectral width, interesting information regarding the Noise can also be retrieved. By way of example, Fig. 18 (top picture) shows the temporal evolution (abscissa) of the retrieved Noise values along a 1° ray as a function of the angle of Elevation (ordinate) for a given RHI (Azimuth set to 56°, from Payerne site) on April 25 (rainy day): at "large" angles of elevation, the radar antenna main lobe intercepts thermal radiation coming mainly from the sky and hydrometeors, depending on the weather conditions. During diurnal hours, the main lobe will also intercept the Sun: in this example, it happens around 13 UTC with an angle of Elevation of approximately 138° (this means an effective Azimuth of 56°+180° = 236° and Elevation of 180-138 = 42); the corresponding pixel in the image is black (saturation in the color palette), since the Sun signal is larger than the visualization threshold set to -104 dBm. (Occasionally, through side-lobes, man-made radiators or other ground features might be detected.) Other values larger than -104 dBm can be seen at low angles of elevation: in this case, thermal radiation intercepted by the antenna comes not only from precipitation but also from the ground. This additional contribution constructively adds to the receiver internal noise and other external radiation; at the end, it results in an increased overall system noise. Hence, low angles of Elevation are characterized by retrieved noise values larger than -106.5 dBm (cyan, green, yellow, orange, red and black, for the given color palette). Can we prove that the increased overall system noise is related to precipitation? The answer is given in the bottom picture of Fig. 18 for an angle of Elevation of 90°: it shows quasi-simultaneous VRP above the DXCH Payerne radar site. The correlation is evident. The lag-time between the RHI (top picture) and the vertical scan (bottom picture) is of the order of few minutes.

In order to be perfectly synchronized, it is also possible to retrieve noise values that are simultaneous with the VRP shown in the bottom picture of Fig. 18. Such values are shown in the last line of Fig. 19, which consists of additional 359 azimuthal noise lines (during the VRP scan the antenna is rotating on itself at 12°/s with PRF = 2000 Hz): as expected, when vertically pointed, the variability of the noise in Azimuth is negligible with respect to the temporal variability, which can be related to the presence of large, falling hydrometeors.

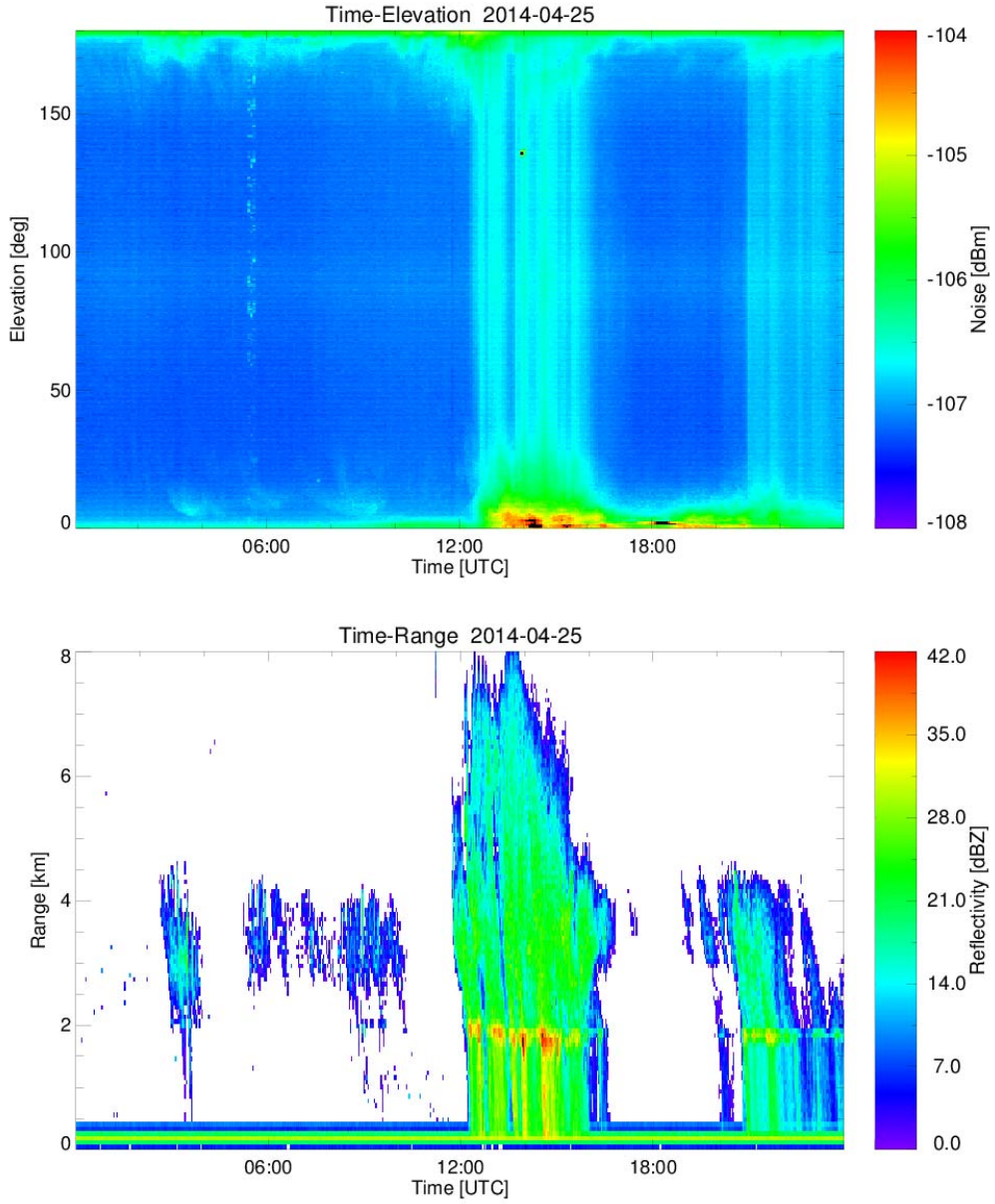

Fig. 18: (top) temporal evolution of the retrieved Noise from Doppler spectra as a function of the angle of Elevation for RHI acquisition with Azimuth set to 56°; (bottom) temporal evolution of the vertical radar reflectivity profile above the DXCH Payerne radar site (to get the altitude above mean sea level it is sufficient to add Payerne site altitude, which is 447 m, to the range values). An increase in the overall system noise aloft (Elevation equal to 90° in the top picture) corresponds to the presence of large hydrometeors

The last example presented in this Sec. 5.4 deals with a comparison between the radial Doppler components detected by the DXCH above Avenches and those retrieved by the echoes acquired at L-band by the mobile vertically pointing wind profiler Lap3000 9P located at Avenches, which is 8.84 km from the DXCH site in Payerne (Azimuth = 56°). Obviously, the DXCH is only sensitive to radial scatterers components. Every 5 minutes the radar is measuring the radial Doppler velocity in direction towards Avenches. During this RHI scan, the upward moving antenna is sampling the moving hydrometeors with a synchronization angle of 1° in elevation and a staggered PRF (1500 and 2000 Hz); the number of DFT samples is 86. The preparatory work for the comparison consists of the following steps (A) for the DXCH and steps (B) for the windprofiler:

- (A) extracting the radial components measured by the weather radar above the location of the wind profiler in Avenches; generating a X-band-based time-height matrix.

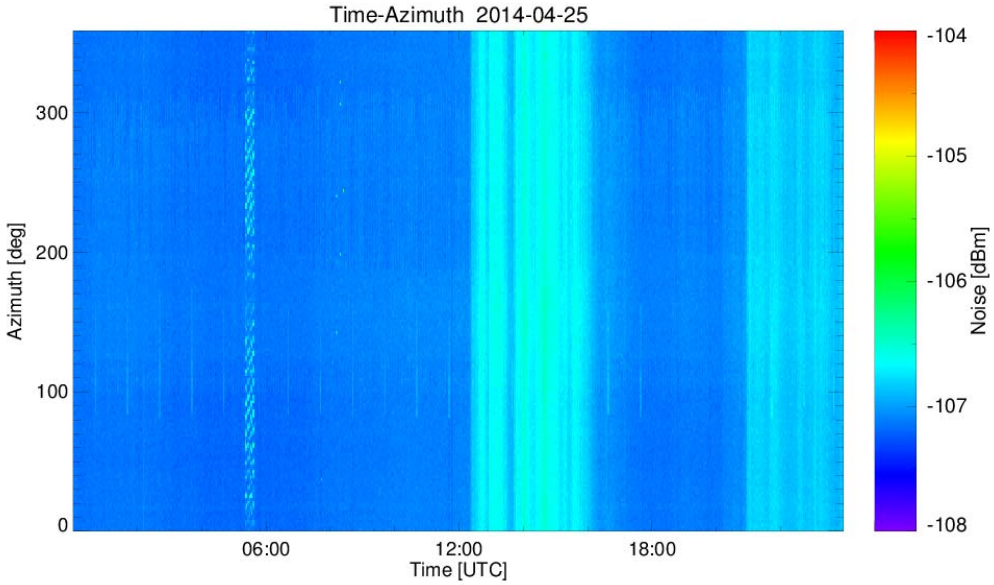

Fig. 19: temporal evolution of the retrieved Noise from Doppler spectra as a function of Azimuthg for a vertically pointing acquisition (see also Fig. 18).

- (B) Projecting the wind vectors retrieved by the wind profiler along the weather radar radial direction; generating a L-band-derived time-height matrix, which can easily be compared visually and numerically with the X-band one.

Figure 20 displays the time-height radar reflectivity matrix of the DXCH above Avenches on April 8, 2014: a rain event is clearly distinguishable from 03 to 12 UTC with echoes up to 8.5 km altitude (8 km height above Payerne site, which is 447 m altitude). Figure 21 shows the DXCH radial velocity field: surprisingly, there are no approaching echoes (blu colors); all scatterers are moving away from the radar; above 4.5 km altitude, some of them (black patches), are even characterized by velocity larger than 20 m/s. The DXCH is obviously not able to detect any Doppler component after the end of the rain event. On the contrary, the wind profiler (1.29 GHz) is able to retrieve information regarding the radial component of the wind even in absence of precipitating hydrometeors detectable by the precipitation radar (10 GHz); this fact can be easily seen in the wind profiler time-height matrix above Avenches shown in Fig. 22.

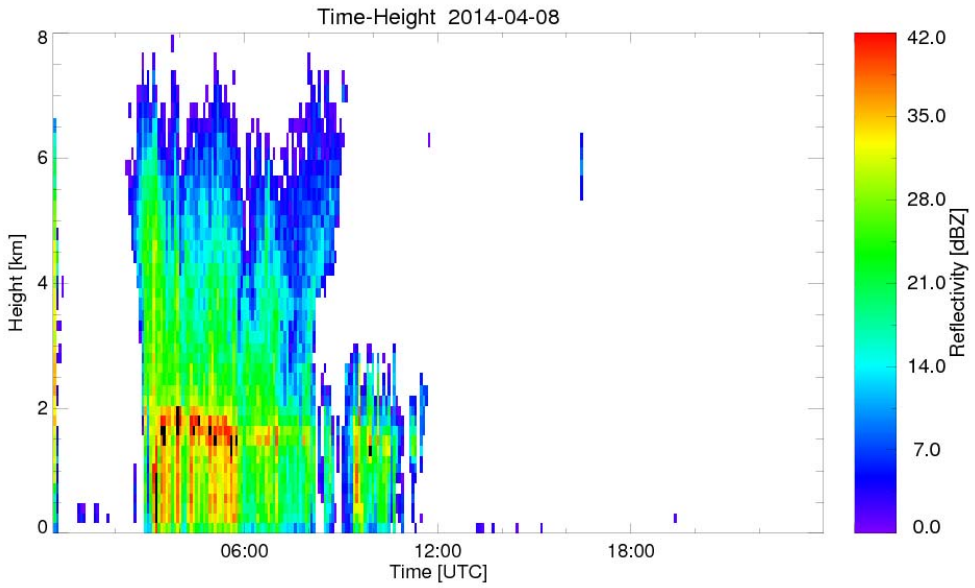

Figure 20: DXCH time-height radar reflectivity above Avenches

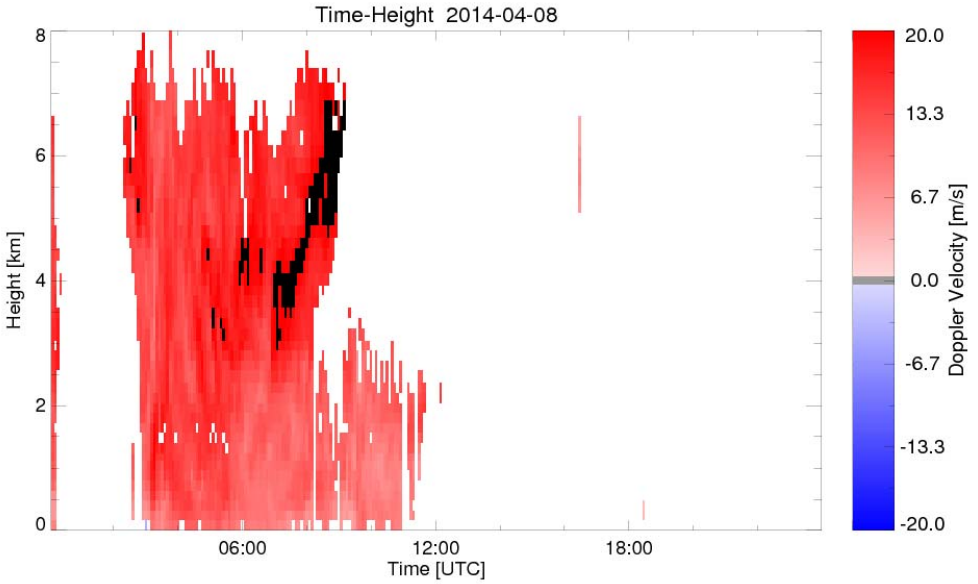

Figure 21: DXCH time-height radial velocity above Avenches

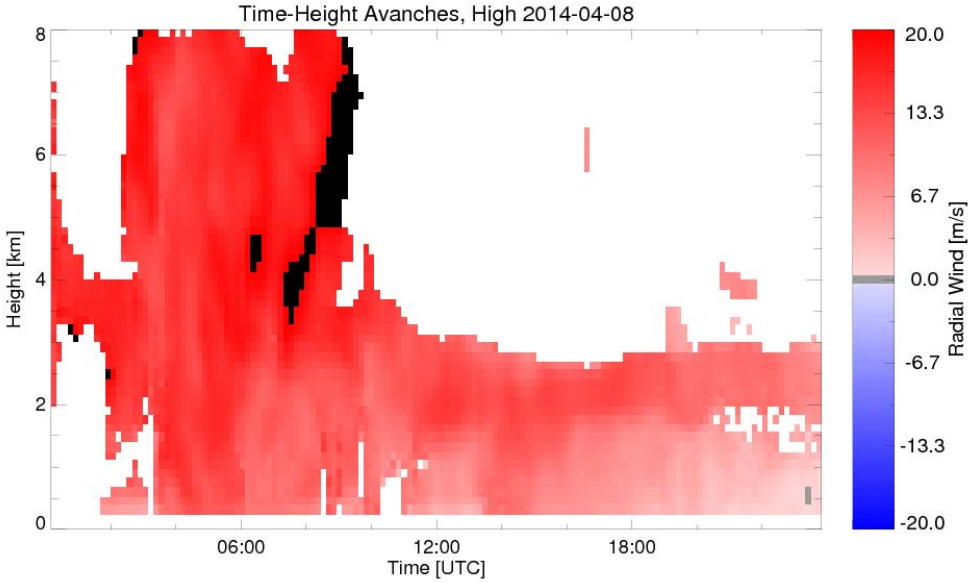

Figure 22: time-height velocity field resulting from the projection along the DXCH radial direction of the wind vectors retrieved by the wind profiler located in Avenches

During the time frame where a comparison is feasible (say, from from 03 to 12 UTC) a visual comparison between the two systems (Fig. 21 vs Fig. 22) is quite satisfactory.
Several other examples and results regarding the DXCH can be found in *Schneebeli et al.* [2013]. More examples will be presented on July 7 at the WMO CIMO TECO 2014 meeting.

6 Conclusions: filling the gap

6.1 Open issues and limitations

X-band radar has the benefit of attaining high spatial resolution with a smaller antenna. However, there is a clear disadvantage compared to longer wavelengths: an increased attenuation in the presence of precipitation. Imagine three 2-km convective cells with instantaneous rain rate of 20, 40 and 100 mm/h respectively: at X-band frequencies these cells would cause two-way attenuation in radar reflectivity values

of approximately 1.5, 3.6 and 11 dB. Such figures preclude not only the use of low-cost, single-pol X-band radar (like the ones presented in Sec. 3) for long-range monitoring but also an accurate QPE, even at short-range. A remedy can be the use of polarimetric information; obviously this increases the cost of the system. To give some figures, the cost of the high-performance system presented in Sec. 5 is almost 13 dB larger than the simple mini-radar described in Section 2. Note also that in the in the interesting and exhaustive paper *Mc Laughlin et. al* [2009], the cost of a Doppler, fully Polarimetric X-band system developed within the framework of the CASA project is estimated 9 dB more expensive than the one described in Sec. 3.

6.2 Filling the gap: X-band radar observations of the lowest part of the troposphere

Current approaches to operational weather observations are based on spaceborne weather radars (the recently launched Global Precipitation Measuring satellite) and (over the continents) on the use of physically large, high-power, long-range radars. In the former case, the main limitation is represented by the limited horizontal resolution; in the latter case, by "range degradation". By the term "range degradation" we mean several important sources of uncertainty regarding radar-based estimates of rainfall: beam broadening, non-homogeneous beam filling, partial beam occultation, overshooting and, depending on the operating frequency, attenuation. Such sources of uncertainty in general increase with increasing range. The radar sampling volume, in fact, increases with the square of the range therefore, at longer ranges, small but intense features of the precipitation system are blurred (non-homogeneous beam filling). Furthermore, it is more likely to include different types of hydrometeors (e.g. snow, ice, hail, rain drops), especially in the vertical dimension. Radar short-wavelength technology is able to fill a gap in observational meteorology: small radars can be used to supplement conventional, long-range radar networks in complex orography regions, in highly populated areas (improving urban hydrology in major towns), in sensitive regions (areas prone to hydro-geological hazards) and along technological networks (e.g. highways, gas pipelines, …) Spacing these radars thirty kilometers apart can help to defeat the Earth's curvature problem and enables the sampling of the lowest part of the troposphere with small antennas and low-power transmitters. This technology has the potential to supplement the widely spaced networks of physically large high-power radars in use today. New spatio-temporal scales (see the last "Summary Table" below), which characterize the highly variable precipitation field can now be investigated at affordable costs thanks to portable/mobile "higher-frequency" weather radars.

Type of device	Band	Cost	Coverage	Sampling vol.	Temporal resol.
GPM dual-frequency spaceborne radar	Ku-Ka		global	$5 \cdot 10^9$-10^{10} m^3	Once per day
Long-range, Doppler, dual-pol radar	S (C)	1000 to 2000 k€	200 000 km^2	10^5-10^9 m^3	300 s
Medium-range, Doppler, dual-pol radar	**X**	200 to **600 k€**	**5000 km^2**	**10^4-10^8 m^3**	**120 s**
Short–range radar	**X**	**30 k€**	**2000 km^2**	**10^4-10^7 m^3**	**60 s**
Rain Gauge	---		point	50 m^3	600 s
Disdrometer	---		point	10 m^3	600 s

Summary Table. The observational gap filled by the innovative X-band systems presented in Sec. 3 and Sec. 5.

ACKNOWLEDGMENTS.
The work was supported by the Swiss Confederation, especially the Federal Department of Defence, Civil Protection and Sport, armasuisse. The authors wish to thank Rudolf Hüppi, Reto König and Alexander Haefele for fruitful and stimulating discussions. Israeli rain gauge data were provided by the Israeli Meteorological Service; analyzed and processed by Anton Lokshin.

REFERENCES

Austin P. M., 1987: Relation between measured radar reflectivity and surface rainfall, *Mon. Weather Rev.*, **115**, 1053–1070.

Gabella M. and G. Perona, 1998: Simulation of the orographic influence on weather radar using a geometric-optics approach, *J. Atm. Oceanic Tech*., **15**, 1486-1495.

Gabella M., Morin E. and R. Notarpietro, 2011: Using TRMM spaceborne radar as a reference for compensating ground-based radar range degradation: Methodology verification based on rain gauges in Israel, *J. Geophys. Res.*, **116**, D02114, doi: 10.1029/2010JD014496.

Germann U. and J. Joss, 2002: Mesobeta profiles to extrapolate radar precipitation measurements above the Alps to the ground level, *J. Appl. Meteorol.*, **40**, 74-89.

Germann U., Galli G., Boscacci M., Bolliger M. and M. Gabella, 2004: Quantitative precipitation estimation in the Alps: where do we stand? Third European Conference on Radar meteorology ERAD2004, Visby, Sweden, 2-6.

Germann U., Galli G., Boscacci M., and M. Bolliger, 2006: Radar precipitation measurement in a mountainous region, *Q. J. Roy. Meteorol. Soc*., **132**, 1669–1692.

Mc Laughlin and other 28 coauthors, 2009: Short-wavelength technology and the potential for distributed networks of small radar systems, *Bull. Am. Meteorol. Soc*., **90**, 1797-1817.

Hogan R.J., O'Connor E. J. and A. J. Illingworth, 2009: Verification of cloud-fraction forecasts, *Q. J. Royal Meteorol. Soc*., **135**, 1494-1511.

Hueppi R., Leunberger A., Schneebeli M., and M. Gabella, 2012: MALS Plus Project: Site Acceptance Tests (SAT) of the DX50 Doppler and polarimetric meteorological radar: SAT protocol, pp. 7.

Joss J., Cavalli R. and R.K. Crane, 1974: Good agreement between theory and experiments for attenuation data, *J. Res. Atmos.*, **8**, 299-318.

Sauvageot H., 1992: *Radar meteorology*, 366 pp., Boston, Artech House.

Schneebeli M., Leunberger A., Figueras J., and M. Gabella, 2013: Meteorological support for the MALS Plus project: measurement concept, MeteoSwiss Tech. Report, pp. 62.

Testud J., E. Le Bouar E. Obligis and M. Ali-Mehenni, 2000: The rain profiling algorithm applied to polarimetric weather radar. J. Atmos. Oceanic Technol., **17**, 332–356.

Tartaglione N., 2010: Relationship between precipitation forecast errors and skill scores of dichotomous forecasts, *Weath. Forec*., **25**, 355-364.

Zawadzki I., 1975: On radar-raingage comparison, *J. Appl. Meteorol*., **14**, 1430-1436.